Spinning test body orbiting around a Schwarzschild black hole: Circular dynamics and gravitational-wave fluxes

Spinning test body orbiting around a Schwarzschild black hole: Circular dynamics and gravitational-wave fluxes

Enno Harms,[1] Georgios Lukes-Gerakopoulos,[2] Sebastiano Bernuzzi,[3] and Alessandro Nagar[4]
[1]*Theoretical Physics Institute, University of Jena, 07743 Jena, Germany*
[2]*Institute of Theoretical Physics, Faculty of Mathematics and Physics, Charles University in Prague, 18000 Prague, Czech Republic*
[3]*DiFeST, University of Parma, and INFN, 43124 Parma, Italy*
[4]*Institut des Hautes Etudes Scientifiques, 91440 Bures-sur-Yvette, France*
(Received 8 September 2016; published 4 November 2016)

We consider a spinning test-body in circular motion around a nonrotating black hole and analyze different prescriptions for the body's dynamics. We compare, for the first time, the Mathisson-Papapetrou formalism under the Tulczyjew spin-supplementary condition (SSC), the Pirani SSC, and the Ohashi-Kyrian-Semerak SSC, and the spinning particle limit of the effective-one-body Hamiltonian of Damour and Nagar [Phys. Rev. D **90**, 044018 (2014).]. We analyze the four different dynamics in terms of the innermost stable circular orbit (ISCO) shifts and in terms of the coordinate-invariant binding energies, separating higher-order spin contributions from spin-orbit contributions. The asymptotic gravitational-wave fluxes produced by the spinning body are computed by solving the inhomogeneous $(2+1)D$ Teukolsky equation and contrasted for the different cases. For small orbital frequencies Ω, all the prescriptions reduce to the same dynamics and the same radiation fluxes. For large frequencies, $x \equiv (M\Omega)^{2/3} > 0.1$, where M is the black hole mass, and especially for positive spins (aligned with the orbital angular momentum) a significant disagreement between the different dynamics is observed. The ISCO shifts can differ by up to a factor of 2 for large positive spins; for the Ohashi-Kyrian-Semerak and the Pirani SSC the ISCO diverges around dimensionless spins $\sim$0.52 and $\sim$0.94, respectively. In the spin-orbit part of the energetics the deviation from the Hamiltonian dynamics is largest for the Ohashi-Kyrian-Semerak SSC; it exceeds 10% for $x > 0.17$. The Tulczyjew and the Pirani SSCs are compatible across almost the whole spin and frequency range. Our results will have direct applications in including spin effects in effective-one-body waveform models for circularized binaries in the extreme-mass-ratio limit.

DOI: 10.1103/PhysRevD.94.104010

I. INTRODUCTION

The motion of a small, spinning test-body on a fixed background is a long-standing problem in general relativity [1,2]. One starts with the idea of representing the motion of the small body by the worldline of a single reference point that lies inside the body, thus motivating the term "spinning point particle." To account for finite-size effects like the *spin*, one usually endows the particle with Mathisson's [1,3,4] "gravitational skeleton": a multipole expansion of the energy-momentum tensor at the reference point that sustains the appearing multipole moments up to some order. In the widely used pole-dipole approximation one truncates this expansion at first order [3,5], neglecting quadrupolar and higher moments [6–10]. The zeroth multipole moments—often called the mass monopole—can be encoded in the four-momenta p_μ, while the first moments—often called the spin-dipole—can be encoded in the antisymmetric spin-tensor $S^{\mu\nu}$. Thus the evolution system for a spinning particle typically comprises the variables

$$\{X^\mu, v^\mu, p_\mu, S^{\mu\nu}\}, \tag{1}$$

where $X^\mu = X^\mu(\lambda)$ is the worldline of the particle, where λ is the proper time and $v^\mu = dX^\mu/d\lambda$ is the tangent vector. The equations of motion (EOM) for this set of variables can be derived from the covariant conservation of energy and momentum, and they are called the "Mathisson-Papapetrou-Dixon" equations (MP) [2,4,11–15].

The MP are not a closed system of equations with respect to the variables (1); they prescribe the evolution of p_μ and $S^{\mu\nu}$, but not of v^μ. Thus, the EOM of a spinning particle are *not* unique. The physical reason is that there is a freedom in choosing the particle's reference point due to the absence of a unique center of mass in general relativity. To remove this ambiguity, one might naively identify the particle with any point inside the body and then directly prescribe its tangent vector at all times. Such an *ad hoc* procedure would, however, be prone to undesired features like a worldline that moves through the body uncontrollably. Instead, a physically robust procedure is to identify the reference point for the particle with the center of mass as perceived by some preferred observer. This point is called "the centroid," and it conventionally serves not only as the reference point for the particle but also as the central point against which the internal rotations of the body (i.e., the spin) are

measured. Hence, selecting a centroid also fixes the particle and its spin. This procedure is realized by enhancing the MP by a *spin-supplementary condition* (SSC). In general, a SSC imposes that $S^{0\mu} = 0$ holds for some preferred observer. Though being at first sight only a condition on the spin, it turns out that $S^{0\mu} = 0$ in fact guarantees that the observer's centroid is identified with the particle and used for measuring the spin [16]. The remaining ambiguity lies thus in the choice of the preferred observer.

Several such SSCs have been used in the literature [4,11,16–20] and their influences on the dynamics have been studied in, e.g., Refs. [16,21]. The variety of EOM for a spinning particle is even larger than the variety of SSCs because, alternatively to the MP, one may take a Hamiltonian approach. Hamiltonian dynamics for a spinning particle were derived in several different forms [22–27]. The mutual relations between the different dynamical approaches are presently not a trivial issue. In Ref. [22] the theoretical equivalence of the (unclosed) MP and the Hamiltonian EOM was shown. However, in practice one has to work with the closed MP, i.e., with some fixed SSC, and one may make a choice other than the Newton-Wigner SSC, for which most of the explicit functions of the Hamiltonian formulation have been derived [22,23,25,27]. Even a numerical comparison of the different dynamical prescriptions is difficult. On the one hand, conclusive comparisons require initial data that corresponds to the same physical situation, which is a highly nontrivial task, e.g., due to the shifts of the different centroids associated with the different SSCs [16]. On the other hand, even when equivalent initial data are found, the respective worldlines of the particle will sooner or later deviate from one another, thus preventing a consistent mutual comparison [16,21]. Furthermore, it has been found numerically that the dynamics of different approaches are compatible for small spins but can diverge for large spins [21]. In fact, it is impossible to say that one dynamical prescription is more appropriate than the others. But one should put forward the questions of how the different formulations relate to each other and whether they lead to different gravitational-wave (GW) signals when applied to the same physical situation.

In this paper we specifically consider the situation of a spinning particle moving on a circular orbit in a nonrotating black hole (BH) background. Such a system can be viewed as a model for a circularized spinning BH binary of extreme mass ratio in which the test body is a *test black hole*. Note though that at the pole-dipole level calling the body a black hole is just a matter of perspective: without accounting for higher multipoles the structure of the object is irrelevant for the dynamics and a black hole cannot be discerned from any other spinning object. In fact, one may expect the higher multipoles to become important in the strong field, where at least the effects from the quadrupole term may become comparable with the effects from the dipole term. Thus, the absence of the higher multipoles can be a reason for the discrepancies between the different prescriptions in the strong field, as will be discussed in the course of this paper.

We analyze and contrast, for the first time, the dynamics and associated GW fluxes obtained when using the

(i) MP with the Tulczyjew (T) SSC [4],
(ii) MP with the Pirani (P) SSC [19],
(iii) MP with the Ohashi-Kyrian-Semerak (OKS) SSC [16,20], and
(iv) a Hamiltonian EOM based on an effective-one-body Hamiltonian with the linearized T SSC [28].

We compare gauge-invariant energetics of circular orbits and the innermost stable circular orbit (ISCO) frequencies. We find that all the dynamics are compatible in terms of the energetics (shown in Figs. 1 and 2) for dimensionless particle spins with absolute value less than 0.2, where a spin with value 1 corresponds to the extremal case when viewing the body as a spinning BH. In this regime of small spins the relative differences in the ISCO shifts are below 20%; see Fig 3. Additionally, we compute the respective asymptotic GW fluxes at null infinity using the time-domain Teukolsky approach of Ref. [29] (hereafter Paper I). As shown in Fig 4, we find that the GW fluxes relative to the different dynamics agree with each other within our numerical precision at low frequencies (large orbital radii). At high frequencies, i.e., small orbital radii close to the respective ISCOs our results, however, indicate that the different dynamics yield significantly different GW fluxes.

The article is organized as follows. In Sec. II we review the MP formalism and the SSCs employed in this work. For all the cases we work out how circular equatorial orbits (CEOs) and the ISCO locations can be found numerically. Similarly, in Sec. III we review the Hamiltonian formalism, and the corresponding CEO and ISCO computations. In Sec. IV we analyze the circular dynamics given by the different EOM using both binding energy curves and the spin-dependent shift of the ISCO frequency. In Sec. V we compare the asymptotic GW fluxes computed at null infinity.

Units and notation: Geometric units are used throughout this work, $G = c = 1$. We use the Riemann tensor defined as $R^{\alpha}{}_{\beta\gamma\delta} = \Gamma^{\alpha}_{\gamma\lambda}\Gamma^{\lambda}_{\delta\beta} - \partial_{\delta}\Gamma^{\alpha}_{\gamma\beta} - \Gamma^{\alpha}_{\delta\lambda}\Gamma^{\lambda}_{\gamma\beta} + \partial_{\gamma}\Gamma^{\alpha}_{\delta\beta}$, where the Christoffel symbols Γ are computed from the metric with signature $(-,+,+,+)$.

We describe a generic binary system with the two masses m_1, m_2 and spin magnitudes S_1, S_2 in the convention that $m_1 \gtrsim m_2$. We define $M \equiv m_1 + m_2$, $\mu \equiv m_1 m_2/M$, and $\nu \equiv \mu/M$. The test-particle limit, which we consider in the numerical experiments of this work, is then understood by $M = m_1 \gg m_2 = \mu$ and $\nu = 0$. More precisely, in the test-particle limit we denote by M the mass of the central BH and by μ the mass of the particle.

In fact, for a spinning particle there are different notions of mass. In most cases considered here the conserved mass

of the particle is defined as $\mu \coloneqq \sqrt{-p^\mu p_\mu}$. Exceptionally, when discussing the MP with the P SSC in Sec. II B, the conserved rest mass is defined differently [see Eq. (6)] and called m. Note that, when using dimensionless quantities that involve the particle's rest mass, one would thus have to use different quantities for the different dynamics, to be strict (see Appendix B). For simplicity we will not do so; instead, we use the same symbols and expect that this subtlety is understood by the reader, e.g., we always denote the dimensionless spin of the particle by σ, which means $\sigma \equiv S_2/(\mathsf{m}M)$ for the P SSC but $\sigma \equiv S_2/(\mu M)$ for the other cases. In practice, in the perturbative calculations both μ and M scale away so that we work numerically with $\mu = M = 1$, and the variable σ varies between $-1 \leq \sigma \leq 1$.

For the Kerr BH background with spin angular momentum $S_1 = a_1 M = \hat{a}_1 M^2$, and its nonspinning Schwarzschild limit, we use the standard Boyer-Lindquist (BL) coordinates $\{t, r, \theta, \phi\}$. In the transition of the effective-one-body (EOB) description for generic binaries to the extreme-mass-ratio limit in Sec. III, we also need the EOB radial coordinate of the deformed Kerr background, r^{EOB}, and we denote its mass-reduced form by $\hat{R} = r^{\mathrm{EOB}}/M$. Note that $r^{\mathrm{EOB}} = r$ only if $\nu = 0$ and $S_1 = 0$, $S_2 = 0$, i.e., even for $\nu = 0, S_1 = 0$ the background is deformed if $S_2 \neq 0$; cf. Sec. IV for more details.

II. MATHISSON-PAPAPETROU DYNAMICS

In the following section we review the MP and discuss how circular orbits can be produced numerically using the MP with either the T SSC, the P SSC, or the OKS SSC. The analogous discussion for the Hamiltonian approach is given in Sec. III.

A. EOM and SSC

The MP in their current standard form read [14]

$$\frac{Dp^\mu}{d\lambda} = -\frac{1}{2} R^\mu{}_{\nu\kappa\lambda} v^\nu S^{\kappa\lambda}, \tag{2a}$$

$$\frac{DS^{\mu\nu}}{d\lambda} = p^\mu v^\nu - v^\mu p^\nu, \tag{2b}$$

where $D/d\lambda \equiv v^\mu \nabla_\mu$. The system of equations (2) is not closed, and a SSC must be specified in order to confine to a unique solution.

A common procedure for finding a SSC stems from our Newtonian intuition that *spin* should be space-like, that is, the spin-tensor should be orthogonal to the four-velocity of some preferred time-like observer. Representing this observer by some future-pointing time-like vector V^μ with

$$V^\mu V_\mu = -1, \tag{3}$$

the general form of a SSC reads

$$V_\mu S^{\mu\nu} = 0. \tag{4}$$

Three of the four conditions (4) are linearly independent, and along with Eq. (3) they fix the centroid that is tracked by the MP. For example, for the T SSC one takes $V^\mu = p^\mu/\mu$ (see below), where μ is the dynamical rest mass

$$\mu \coloneqq \sqrt{-p^\mu p_\mu}. \tag{5}$$

For later reference, we also introduce here another notion of mass,

$$\mathsf{m} \coloneqq -v^\mu p_\mu, \tag{6}$$

which is important for the P SSC.

In general, the particle's four-momentum p_μ and four-velocity v^μ are not parallel. If they were, we would have $\frac{DS^{\mu\nu}}{d\lambda} = 0$ from Eq. (2b). In fact, rearranging that equation, one gets

$$p^\mu = \mathsf{m} v^\mu - v_\nu \frac{DS^{\mu\nu}}{d\lambda}, \tag{7}$$

where the second term is known as the *hidden* momentum, i.e.,

$$p^\mu_{\mathrm{hidden}} \coloneqq p^\mu - \mathsf{m} v^\mu \tag{8}$$

(see, e.g., Refs. [31,32]). As discussed below, the OKS SSC is characterized by $p^\mu_{\mathrm{hidden}} = 0$.

Having defined the observer's reference vector V^μ, it is possible to introduce the spin four-vector

$$S_\mu = -\frac{1}{2} \epsilon_{\mu\nu\rho\sigma} V^\nu S^{\rho\sigma}, \tag{9}$$

where $\epsilon_{\mu\nu\rho\sigma} = \sqrt{-g}\tilde{\epsilon}_{\mu\nu\rho\sigma}$ is the Levi-Civita tensor with the Levi-Civita symbol $\tilde{\epsilon}_{0123} = 1$ and the determinant g of the background metric tensor. The inversion of Eq. (9) reads

$$S^{\rho\sigma} = -\epsilon^{\rho\sigma\gamma\delta} S_\gamma V_\delta, \tag{10}$$

and the spin's magnitude is

$$S^2 = \frac{1}{2} S^{\mu\nu} S_{\mu\nu} = S^\mu S_\mu. \tag{11}$$

The constancy of the scalar quantities μ, m, and S depends on the choice of the SSC, and it is summarized in Table I. For instance, for the T SSC, μ is constant but m is not, and vice versa for the P SSC [33]. For the OKS SSC both notions of mass are constant [16]. In general, the spin magnitude S is not constant upon evolution, but it is constant for all SSCs discussed here (see, e.g., Refs. [16,33]).

TABLE I. Constancy of the two notions of mass μ [Eq. (5)] and m [Eq. (6)], and of the spin magnitude S [Eq. (11)], for the Tulczyjew (T) SSC, the Pirani (P) SSC, and the Ohashi-Kyrian-Semerak (OKS) SSC. Constancy is denoted by a ✓, whereas × marks that the quantity is not constant. For more details some references to appearances of these SSCs in the literature are included.

SSC	V^μ	μ	m	S	References
T	Eq. (15)	✓	×	✓	[4,16,21,33–35]
P	Eq. (18)	×	✓	✓	[16,19,33,35]
OKS	Eq. (22)	✓	✓	✓	[16,20,31]

Besides the SSC-dependent constants of motion, there are more general, background-dependent constants constructed from Killing vectors. In particular, for a Killing vector ξ^μ the quantity

$$C = \xi^\mu p_\mu - \frac{1}{2}\xi_{\mu;\nu}S^{\mu\nu} \tag{12}$$

remains conserved upon evolution [12]. For stationary and axisymmetric spacetimes with a reflection symmetry along the equatorial plane (SAR spacetimes) we have, using BL coordinates, the two Killing vector fields $\xi^\mu_{(t)} = \delta^\mu{}_t$ and $\xi^\mu_{(\phi)} = \delta^\mu{}_\phi$. The corresponding conserved quantities are

$$E := -p_t + \frac{1}{2}g_{t\mu,\nu}S^{\mu\nu}, \tag{13}$$

and

$$J_z := p_\phi - \frac{1}{2}g_{\phi\mu,\nu}S^{\mu\nu}, \tag{14}$$

respectively. $E = \text{const}$ corresponds to the conservation of energy and $J_z = \text{const}$ to the conservation of the component of the total angular momentum along the symmetry axis z.

In the following we briefly introduce the SSCs used in this work. A thorough analysis of these conditions can be found in Refs. [16] and [31].

1. Tulczyjew SSC

For the T SSC [4] the reference vector is

$$V^\mu = \frac{p^\mu}{\mu}. \tag{15}$$

This choice makes the spin spatial for an observer moving in the direction of the four-momentum,

$$p_\mu S^{\mu\nu} = 0 \qquad (\text{T SSC}). \tag{16}$$

For the T SSC an explicit relation between v^μ and p_μ, $S^{\mu\nu}$ can be found, i.e.,

$$v^\mu = \frac{\mathsf{m}}{\mu^2}\left(p^\mu + \frac{2S^{\mu\nu}R_{\nu\rho\kappa\lambda}p^\rho S^{\kappa\lambda}}{4\mu^2 + R_{\alpha\beta\gamma\delta}S^{\alpha\beta}S^{\gamma\delta}}\right). \tag{17}$$

The T SSC is widely used in numerical applications (e.g., Refs. [35–38]). In particular, in Paper I, we have already discussed the T SSC (cf. Sec. II C therein) and computed the GW fluxes produced by a spinning particle in circular orbits.

2. Pirani SSC

For the P SSC [19] the reference vector is the four-velocity, i.e.,

$$V^\mu = v^\mu, \tag{18}$$

making spin spatial for an observer moving in the direction of the particle's four-velocity,

$$v_\mu S^{\mu\nu} = 0 \qquad (\text{T SSC}). \tag{19}$$

Note that sometimes this choice is called the "Frenkel" SSC [35]. The evolution equation of the four-velocity for the P SSC is given by

$$\frac{Dv^\mu}{d\lambda} = -\frac{1}{S^2}\left(\frac{A}{2m}S^\mu + p_\kappa S^{\mu\kappa}\right), \tag{20}$$

where

$$A = -\frac{R_{\mu\nu\kappa\lambda}S^\mu v^\nu S^{\kappa\lambda}}{2\mathsf{m}S^2}. \tag{21}$$

For the derivation of the equation see, e.g., Ref. [16].

3. Ohashi-Kyrian-Semerak SSC

The OKS SSC was proposed in Refs. [16,20] and revised recently in Ref. [31]; we work with the latter version. The main idea of the OKS SSC is to exploit the freedom in the choice of the future-pointing time-like vector V^μ to impose desirable features on the EOM, like the cancellation of the hidden momentum. To fulfill the OKS SSC upon evolution, one promotes V^μ to an evolution variable of the system and deduces an evolution equation for it. The latter is then solved with suitable initial data.

In the OKS framework the covariant derivative of the time-like four-vector, $DV^\mu/d\lambda$, has to be proportional to S^μ and satisfy the condition

$$\frac{DV_\mu}{d\lambda}S^{\mu\nu} = 0 \qquad (\text{OKS SSC}). \tag{22}$$

Of course, $V_\mu S^{\mu\nu} = 0$ has to hold as well. The condition (22) eliminates the hidden momentum, and therefore

$$p^\mu = \mathsf{m} v^\mu. \tag{23}$$

Once the latter holds, it is straightforward that

$$\mu = \mathsf{m}. \tag{24}$$

According to Ref. [31] a "natural" way to restrict the possible V^μ is to require $\frac{D(v^\mu S_\mu)}{d\lambda} = 0$. Then one can deduce the evolution equations for V^μ,

$$\frac{DV^\mu}{d\lambda} = \frac{\alpha}{\mathsf{m}\mu^2} S^\mu, \tag{25}$$

and for S^μ,

$$\frac{DS^\mu}{d\lambda} = \frac{\alpha S^2}{\mathsf{m}\mu^2} V^\mu, \tag{26}$$

respectively, where

$$\alpha = \frac{\mu^2}{S^2} \frac{Dp^\mu}{d\lambda} S_\mu. \tag{27}$$

For the derivation of Eqs (25) and (26), see Ref. [31]. Note that the OKS SSC does not specify a unique worldline itself unless an initial V^μ has been set.

B. Circular equatorial orbits

The problem of finding CEOs reduces to selecting appropriate initial data for the variables $\{X^\mu, v^\mu, p_\mu, S^{\mu\nu}\}$ so that circular equatorial motion is obtained upon evolution of the MP. In the following, we describe methods for producing such CEO initial data valid for arbitrary SAR spacetimes. We first discuss the part that is common to all the SSCs and then specify the details for each choice of SSC. Additionally, for each SSC we discuss how to determine the ISCO. The latter problem is nontrivial because, as we shall see, the relations between v^μ and p_μ and the constants of motion E and J_z can become complicated. A new procedure to find CEOs and ISCOs is presented for the P and the OKS SSC. Before going into detail, note that, in order to allow eternal circular motion, our setup completely neglects self-force effects of the small body, which (like the spin-curvature coupling of the MP) in principle lead to deviations from geodesic motion [39].

Coordinates: Without loss of generality, we identify the time coordinate of the particle with the background coordinate time t. For the spatial coordinates we set the initial data according to the assumptions that

$$r = \text{const}, \qquad \theta = \frac{\pi}{2}, \qquad \phi = \Omega t. \tag{28}$$

Here $\Omega \equiv d\phi/dt$ is the orbital frequency of the particle, which is expected to remain constant during the evolution, and whose initial data will be determined below from the tangent vector. Note that in Eq. (28) we are not introducing a distinct notation for the particle's coordinates and the background coordinates, respectively; e.g., we simply write r for the particle's BL radius, assuming that the meaning is always comprehensible from the context.

Tangent vector: It is clear that for CEOs we need

$$v^r = 0, \qquad v^\theta = 0, \tag{29}$$

which we therefore set in the initial data. It is not trivial though how $v^t(t=0)$ and $v^\phi(t=0)$ should be determined. In fact, it turns out that the procedures depend on the choice of the SSC and will therefore be discussed separately for each SSC below. Nevertheless, since the time coordinate of the particle is identified with the background coordinate time, v^t is just the lapse of the particle and the relation

$$v^t = \frac{1}{\sqrt{-g_{tt} - 2g_{t\phi}\Omega - g_{\phi\phi}\Omega^2}} \tag{30}$$

is always fulfilled for our calculations.

Four-momentum: The treatment of p^μ depends on the choice of the SSC and it is not always necessary to make additional assumptions on the momenta. For example, if a SSC entails $p^\mu \| v^\mu$, Eq. (29) already implies that the momenta in the radial and polar directions vanish. As a matter of fact, inspecting our dynamical data *a posteriori*, we find that all SSCs tested here share the common feature that

$$p_r = 0, \qquad p_\theta = 0. \tag{31}$$

The reasons are discussed below for each SSC separately.

Spin tensor: We demand that the spin vector of the particle is aligned with the orbital angular momentum,

$$S^\mu = S^\theta \delta^\mu{}_\theta. \tag{32}$$

Note that Eq. (32) combined with Eq. (29) imply that the condition

$$v^\mu S_\mu = 0 \tag{33}$$

is met for all three SSCs that we consider. This is obvious for the P SSC, but it can be shown also for the T SSC (e.g., Ref. [35]) and it can be demanded for the OKS SSC.

The spin vector (32) can be expressed through the spin magnitude S using Eq. (11), which gives

$$S_\theta = -\sqrt{g_{\theta\theta}} S, \tag{34}$$

with $S > 0$ ($S < 0$) corresponding to a spin vector that is (anti)aligned with the orbital angular momentum, which by convention is always pointing along the positive z direction in our setup.

Inserting the assumption (32) into Eq. (10), we get a general prescription for setting the spin tensor,

$$S^{tr} = -SV_\phi\sqrt{-\frac{g_{\theta\theta}}{g}} = -S^{rt}, \tag{35a}$$

$$S^{t\phi} = SV_r\sqrt{-\frac{g_{\theta\theta}}{g}} = -S^{\phi t}, \tag{35b}$$

$$S^{r\phi} = -SV_t\sqrt{-\frac{g_{\theta\theta}}{g}} = -S^{\phi r}, \tag{35c}$$

which we use for all three SSCs by replacing the vector V_μ accordingly; see Sec. II A. Note that at this stage the initial data of V_μ for the OKS SSC are still missing, and they are discussed in Sec. II B 3.

Energy and angular momentum constants: With the relations (35) the constants E and J_z, given by Eqs. (13) and (14), can be written as

$$J_z = p_\phi + \frac{\sqrt{g_{\theta\theta}}}{2\sqrt{-g}}S(g_{t\phi,r}V_\phi - g_{\phi\phi,r}V_t), \tag{36}$$

$$E = -p_t + \frac{\sqrt{g_{\theta\theta}}}{2\sqrt{-g}}S(g_{t\phi,r}V_t - g_{tt,r}V_\phi). \tag{37}$$

Using these equations we are able to specify initial data for (E, J_z) instead of (p_t, p_ϕ).

The procedures to set the remaining initial conditions for CEOs are now discussed separately for each SSC.

1. Tulczyjew SSC

To find CEOs under the T SSC, one replaces $V^\mu = p^\mu/\mu$ in Eqs. (36) and (37), and rearranges the equations such that p_t and p_ϕ are functions of E, J_z, and r. The rearranged equations are plugged into the time and azimuthal components of Eq. (17) to get v^t and v^ϕ as functions of E, J_z, S, and r. The above v^t and v^ϕ are then inserted into the normalization constraint $v^\mu v_\mu = -1$, which is rearranged so that one gets

$$v^r \propto \sqrt{V_{\mathrm{eff,T}}}, \tag{38}$$

where the function $V_{\mathrm{eff,T}} = V_{\mathrm{eff,T}}(E, J_z, S, r)$ is an *effective potential*, by analogy with the effective potential used for a nonspinning particle; see Appendix A. The explicit form of $V_{\mathrm{eff,T}}$ can be found in Eq. (20) of Paper I.

Motion can take place only when $V_{\mathrm{eff,T}} \geq 0$. For $V_{\mathrm{eff,T}} = 0$ one gets the turning points of the motion in the radial direction. However, CEOs have fixed radii, which means that the turning points should also be extrema of $V_{\mathrm{eff,T}}$. Thus, for a CEO it holds that

$$V_{\mathrm{eff,T}} = 0, \qquad \frac{dV_{\mathrm{eff,T}}}{dr} = 0. \tag{39}$$

The solution of the system (39) for a given radial distance r and spin S provides the energy E and the z component of the total angular momentum J_z. For the Kerr background the solution of the system (39) has been found analytically; see, e.g., Refs. [35,40].

An ISCO is a CEO located at an inflection point of the effective potential, in our case of $V_{\mathrm{eff,T}}$. Thus, to find an ISCO's r, E, and J_z for a given spin S, we solve the system (39) along with the condition $\frac{d^2V_{\mathrm{eff,T}}}{dr^2} = 0$.

2. Pirani SSC

In contrast to the single effective potential used to find CEOs for the T SSC, the CEOs for the P SSC are determined here using three "potentials" named V_{P}, $V_{\mathrm{eff},P}$, and $V_{\mathrm{con},P}$.

For equatorial motion in a SAR spacetime it holds that $A = 0$ [cf. Eq. (21)]. Furthermore, once we demand $v^r = 0$ and $p^r = 0$, Eq. (20) implies that the polar acceleration vanishes, $dv^\theta/d\lambda = 0$, as well as the time component $dv^t/d\lambda$ and the azimuthal component $dv^\phi/d\lambda$. The radial component of Eq. (20) is reduced to

$$\frac{dv^r}{d\lambda} = -\frac{V_{\mathrm{P}}}{2S\sqrt{-g}}, \tag{40}$$

where we define

$$V_{\mathrm{P}} \coloneqq 2g_{rr}\sqrt{g_{\theta\theta}}(g_{\phi\phi}v^\phi p_t - g_{tt}v^t p_\phi + g_{t\phi}(v^t p_t - v^\phi p_\phi)) - S\sqrt{-g}\left(\frac{\partial g_{tt}}{\partial r}v^{t2} + 2v^t v^\phi\frac{\partial g_{t\phi}}{\partial r} + \frac{\partial g_{\phi\phi}}{\partial r}v^{\phi 2}\right), \tag{41}$$

in which p_t and p_ϕ are replaced using Eqs. (36) and (37). The condition $V_{\mathrm{P}} = 0$ prevents radial acceleration.

As for the T SSC, the four-velocity contraction provides an effective potential, $V_{\mathrm{eff},P}$. Rearranging $v^\mu v_\mu = -1$ to express the radial velocity v^r as a function of v^t, v^ϕ, and r, one gets

$$v^r = \pm\sqrt{\frac{V_{\mathrm{eff},P}}{g_{rr}}}, \tag{42}$$

where

$$V_{\mathrm{eff},P} \coloneqq -(g_{tt}v^{t2} + 2g_{\phi\phi}v^t v^\phi + g_{t\phi}v^{\phi 2} + 1). \tag{43}$$

Motion is allowed only when $V_{\mathrm{eff},P} \geq 0$.

Finally, by rewriting the definition of the mass m to express the function $v^r p_r$ in terms of v^t, v^ϕ, p_t, and p_ϕ, one obtains

$$V_{\mathrm{con,P}} \coloneqq v^r p_r = -\mathsf{m} - v^t p_t - v^\phi p_\phi. \tag{44}$$

In the above expression p_t and p_ϕ are replaced by Eqs. (36) and (37), in which for the P SSC $V^t = v^t$, $V^\phi = v^\phi$. Thus, $V_{\rm con,P} = V_{\rm con,P}(v^t, v^\phi, r, S, E, J_z)$, which gives the third potential.

To find CEOs for a given r and S, we solve the system

$$V_{\rm eff,P} = 0, \qquad V_{\rm P} = 0, \qquad V_{\rm con,P} = 0,$$
$$\frac{dV_{\rm eff,P}}{dr} = 0, \qquad \frac{dV_{\rm P}}{dr} = 0, \qquad \frac{dV_{\rm con,P}}{dr} = 0, \quad (45)$$

where we consider v^t, v^ϕ as functions of r. Thus, in the latter system the variables are $v^t, v^\phi, dv^t/dr, dv^\phi/dr, \hat{E}$, and $\hat{J}_z$. As far as we know, there are no analytical solutions for CEOs in the literature for the P SSC, and the above numerical procedure is novel. Note that our numerical findings show that this procedure can avoid the helical motion appearing in studies that use the MP with the P SSC [16]. Helical motion was the reason that the P SSC was considered unphysical for a long time. This misconception has been explained in Ref. [41], where it has been shown that the P SSC is physically acceptable.

Here, the ISCO can be found by searching for inflection points of the three potentials. For a given S we solve the system (45) plus

$$\frac{d^2V_{\rm eff,P}}{dr^2} = 0, \qquad \frac{d^2V_{\rm P}}{dr^2} = 0, \qquad \frac{d^2V_{\rm con,P}}{dr^2} = 0, \quad (46)$$

where the variables are $r, v^t, v^\phi, dv^t/drdv^t/dr, dv^\phi/dr, dv^\phi/dr, d^2v^t/dr^2, d^2v^\phi/dr^2, E$, and J_z.

3. Ohashi-Kyrian-Semerak SSC

For the OKS SSC there is no procedure in the literature describing how to find CEOs. We present here a working solution, following the ideas applied for the T SSC and the P SSC. We note that our general demands for CEOs, Eqs. (29) and (32), are compatible with the OKS condition (22). To see this, note that Eqs. (29) and (32) already imply $v^\mu S_\mu = 0$, which is even stronger than the OKS requirement $\frac{D(v^\mu S_\mu)}{d\lambda} = 0$.

For equatorial motion in a SAR spacetime it holds that $\alpha = 0$ [cf. Eq. (27)]. Since $\alpha = 0$, Eqs. (25) and (26) imply that V^μ and S^μ are parallel transported along the worldline, i.e.,

$$\frac{DV^\mu}{d\lambda} = 0 \quad (47)$$

and

$$\frac{DS^\mu}{d\lambda} = 0. \quad (48)$$

Before we proceed, the conservation of the ansatz (32) in time has to be checked for the OKS SSC. From Eq. (48) we get identities $0 = 0$, apart from the θ component which reads

$$\frac{dS^\theta}{d\lambda} + \frac{S^\theta v^r}{r} = 0. \quad (49)$$

From the latter we confirm that if $v^r = 0$, then S^θ is constant. Thus, our ansatz also holds upon evolution for the OKS SSC.

As discussed in Sec. II A 3, we can exploit the fact that V^μ is a relatively arbitrary future-pointing time-like vector in order to get desired features, and this is what we do in order to get CEOs. First we note that the θ component of Eq. (47) gives

$$\frac{dV^\theta}{d\lambda} + \frac{V^\theta v^r}{r} = 0.$$

We can simply impose

$$V^\theta = 0, \quad (50)$$

which is certainly a natural choice for CEOs since the motion takes place on the equatorial plane.

As in the case of the P SSC, we have to use three "potentials." The effective potential comes from the four-velocity contraction, or for the OKS SSC equivalently from the four-momentum contraction $p^\mu p_\mu = -\mu^2$. Namely,

$$p_r = \pm\sqrt{\frac{V_{\rm eff,OKS}}{g^{rr}}}, \quad (51)$$

where

$$V_{\rm eff,OKS} = -(\mu^2 + {p_t}^2 g^{tt} + {p_\phi}^2 g^{\phi\phi} + 2p_t p_\phi g^{t\phi}). \quad (52)$$

In Eq. (52) p_t and p_ϕ have to be replaced using Eqs. (36) and (37) in order to make $V_{\rm eff,OKS}$ a function of r, S, V_t, V_ϕ, E, and J_z. Notably, $V_{\rm eff,OKS}$ does not depend on the V_r component, which means that for simplicity we can set

$$V_r = 0. \quad (53)$$

In fact this requirement is rather convenient since it gives us a relation between V_t and V_ϕ through the fact that $V^\mu V_\nu = -1$ (recall that we have set $V_\theta = 0$), i.e.,

$$V_{\rm OKS1} = 1 + g^{tt}{V_t}^2 + g^{\phi\phi}{V_\phi}^2 + 2g^{t\phi}V_t V_\phi = 0, \quad (54)$$

and, thus, we have the second potential. The requirements $V_r = 0$ and $v^r = 0$ reduce the time and the azimuthal components of Eq. (47) to $\frac{DV_t}{d\lambda} = 0$ and $\frac{DV_\phi}{d\lambda} = 0$, while the radial component gives us the third potential. Namely,

$$\frac{dV_r}{d\lambda} = \frac{V_{\rm OKS2}}{2\mu({g_{t\phi}}^2 - g_{\phi\phi}g_{tt})^2}, \quad (55)$$

where

$$V_{\rm OKS2} = V_\phi\Big((g_{t\phi}p_t - g_{tt}p_\phi)\Big(g_{t\phi}\frac{\partial g_{t\phi}}{\partial r} - g_{tt}\frac{\partial g_{\phi\phi}}{\partial r}\Big) - (g_{\phi\phi}p_t - g_{t\phi}p_\phi)\Big(g_{t\phi}\frac{\partial g_{tt}}{\partial r} - g_{tt}\frac{\partial g_{t\phi}}{\partial r}\Big)\Big) + V_t\Big((g_{\phi\phi}p_t - g_{t\phi}p_\phi)\Big(g_{\phi\phi}\frac{\partial g_{tt}}{\partial r} - g_{t\phi}\frac{\partial g_{t\phi}}{\partial r}\Big) - (g_{t\phi}p_t - g_{tt}p_\phi)\Big(g_{\phi\phi}\frac{\partial g_{t\phi}}{\partial r} - g_{t\phi}\frac{\partial g_{\phi\phi}}{\partial r}\Big)\Big), \quad (56)$$

which we demand to be zero, i.e., we demand that $dV_r/d\lambda = 0$ so that $V_r = 0$ remains satisfied in time.

To find the turning points for a given radius r and spin S, one has to solve the system

$$V_{\rm eff,OKS} = 0, \qquad V_{\rm OKS1} = 0, \qquad V_{\rm OKS2} = 0, \quad (57)$$

so that one of the variables V_t, V_ϕ, E, or J_z can be expressed as a function of the other three. The procedures to find CEOs and the ISCOs are similar to the procedures described in Sec. II B 2 for the P SSC. In particular, we find CEOs for a given r and S by solving the system of the three potentials and their first derivatives with respect to r, where the unknowns are $V_t, V_\phi, dV_t/dr, dV_\phi/dr, E$, and J_z. The ISCOs are found for a given S by solving the system of the three potentials and their first and second derivatives with respect to r, where the unknowns are $V_t, V_\phi, dV_t/dr$, $dV_\phi/dr, d^2V_t/dr^2, d^2V_\phi/dr^2, E$, and J_z.

III. CIRCULAR DYNAMICS OF THE EFFECTIVE-ONE-BODY HAMILTONIAN

The Hamiltonian of a spinning particle on a Kerr BH, written in a certain coordinate system and spin gauge, was obtained in Ref. [22] at linear order in the spin, and it has been used, for example, to incorporate spin effects into the EOB model of Refs. [42–44]. Recently that Hamiltonian was improved to quadratic order in Ref. [27]. By contrast, here we shall use the spinning-particle Hamiltonian obtained from the EOB Hamiltonian for nonprecessing spinning BHs of masses m_1, m_2 and dimensionful spins S_1, S_2 as introduced in Ref. [28] (see Ref. [45] for the precessing version). For the application to our test-particle setup we consider the following limits: (i) one body is much heavier than the other one, $m_1 \gg m_2$; (ii) the heavier body is nonspinning, $S_1 = 0$; (iii) we restrict to circular dynamics; (iv) we only consider spin-orbit couplings and drop spin-spin ones. This yields a rather simplified description of the dynamics, since the EOB Hamiltonian of Ref. [28] includes both spin-orbit (odd-in-spin) and spin-spin (even-in-spin) interactions in a resummed form, i.e., it incorporates an infinite number of spin-spin and spin-orbit couplings. We anticipate in passing that in another ongoing work, which will be published elsewhere, the equivalence between the circular dynamics entailed by the Hamiltonians of Refs. [22,27] and the EOB-based Hamiltonian used here will be checked explicitly.

For completeness, let us recall the structure of the complete EOB Hamiltonian and how to get the spinning test-particle limit from it (see also Sec. II of Ref. [26]). We warn the reader that in the following several EOB-related quantities will be introduced without detailed explanation or discussion. This is done because the spinning test-particle limit of the EOB Hamiltonian of Ref. [28] was not previously studied in our context and we think it is pedagogically useful to derive it from first principles, thus allowing an easy generalization to the Kerr case in the future. Using the notation $M = m_1 + m_2$, $\mu = m_1 m_2/M$, $\nu = \mu/M$, it is first written as

$$H = M\sqrt{1 + 2\nu\Big(\frac{H_{\rm eff}}{\mu} - 1\Big)}, \quad (58)$$

where the effective Hamiltonian $H_{\rm eff}$ for equatorial dynamics of parallel-spin binary systems reads

$$H_{\rm eff} \equiv H^{\rm SO}_{\rm eff} + H^{\rm orb}_{\rm eff} = G^{\rm phys}_S P_\phi S + G^{\rm phys}_{S_*} P_\phi S_* + H^{\rm eff}_{\rm orb}, \quad (59)$$

where P_ϕ is the total orbital angular momentum of the system, while S and S_* are the following symmetric combinations of the two spins:

$$S \equiv S_1 + S_2 = m_1 a_1 + m_2 a_2 = m_1^2 \hat{a}_1 + m_2^2 \hat{a}_2, \quad (60)$$

$$S_* \equiv \frac{m_2}{m_1}S_1 + \frac{m_1}{m_2}S_2 = m_2 a_1 + m_1 a_2 = m_1 m_2(\hat{a}_2 + \hat{a}_2). \quad (61)$$

The orbital effective Hamiltonian is

$$H^{\rm eff}_{\rm orb} = \sqrt{A\Big(\mu^2 + \frac{L^2}{r_c^2} + Q_4\Big) + P^2_{r^{\rm EOB}_*}}, \quad (62)$$

where r_c^2 is the squared centrifugal radius (that encodes here for simplicity only leading-order spin-spin couplings)

$$r_c^2 \equiv r^2_{\rm EOB} + a_0^2\Big(1 + \frac{2M}{r_{\rm EOB}}\Big), \quad (63)$$

where, as mentioned before, $r_{\rm EOB}$ is the radial EOB coordinate. The spin combination

$$a_0 = a_1 + a_2 \quad (64)$$

is the effective Kerr parameter, while $G_S^{\rm phys}(r_{\rm EOB}, m_1, m_2, S_1, S_2)$ and $G_{S_*}^{\rm phys}(r_{\rm EOB}, m_1, m_2, S_1, S_2)$ are the two spin-orbit coupling functions. In addition, in Eq. (62) we have the radial potential $A(r_{\rm EOB}, m_1, m_2, S_1, S_2)$, the function $Q_4 \equiv 2\nu(4-3\nu)p_{r_*}^4 u_c^2$, and the radial momentum $P_{r_*^{\rm EOB}} \equiv \sqrt{A/B}P_{r^{\rm EOB}}$ (canonically conjugate to a certain tortoise-like radial coordinate $r_*^{\rm EOB}$), which introduces the second EOB potential function $B(r_{\rm EOB}, m_1, m_2, S_1, S_2)$. In this framework, the dynamics is determined by the structure of the functions $(A, B, G_{S_*}^{\rm phys}, G_S^{\rm phys})$ (for example, as defined in Refs. [28]), and they are chosen so as to incorporate explicitly the (spinning) test-particle limit. Going now to the circular limit, $P_{r_*^{\rm EOB}} = 0$, and defining the dimensionless versions of the spin-orbit coupling functions $G_S \equiv M^3 G_S^{\rm phys}$ and $G_{S_*} \equiv M^3 G_{S_*}^{\rm phys}$, as well as the dimensionless quantities $\hat{H}_{\rm eff} \equiv H_{\rm eff}/\mu$ and $\hat{P}_\phi \equiv P_\phi/(M\mu)$, we have

$$\hat{H}_{\rm eff} = G_S \hat{P}_\phi S + G_{S_*}\hat{P}_\phi S_* + \sqrt{A(1+\hat{P}_\phi^2 U_c^2)}, \tag{65}$$

where

$$U_c^2 \equiv \left(\frac{M}{r_c}\right)^2 \equiv \frac{U^2}{1+\hat{a}_0^2 U^2(1+2U)}, \tag{66}$$

and $\hat{a}_0 \equiv a_0/M$. Here we have defined the inverse EOB radial coordinate

$$U \equiv M/r_{\rm EOB} \equiv 1/\hat{R}, \tag{67}$$

whose relation to the standard Schwarzschild radial coordinate $\hat{r} \equiv r/M$ will be discussed below in Sec. III D. Replacing (S, S_*) with the dimensionless spin variables $(\hat{a}_1, \hat{a}_2)$, one has

$$\hat{H}_{\rm eff} = \hat{P}_\phi\{[(X_1)^2\hat{a}_1 + (X_2)^2\hat{a}_2]G_S + \nu(\hat{a}_1+\hat{a}_2)G_{S_*}\} + \sqrt{A(1+\hat{P}_\phi^2 U_c^2)}, \tag{68}$$

where $X_{1,2} = m_{1,2}/(m_1+m_2)$. Let us now go to the limit where one mass is much smaller than the other one, $\mu \equiv m_2 \ll M \equiv m_1$, so that we have $\hat{H} = H/\mu = \hat{H}_{\rm eff}$. At this stage we still allow $(\hat{a}_1, \hat{a}_2) \neq 0$, i.e., we keep also the leading-order term (in the mass ratio) proportional to $\hat{a}_1$, so as to consider a *spinning* particle on a Kerr background. Explicitly focusing only on the spin-orbit part, from $X_1 \to 1$ and $X_2 \to m_2/m_1$ one gets

$$\hat{H}_{\rm SO} \approx \hat{P}_\phi\left\{G_S\left[\hat{a}_1 + \left(\frac{m_2}{m_1}\right)^2\hat{a}_2\right] + G_{S_*}\frac{m_2}{m_1}(\hat{a}_1+\hat{a}_2)\right\}, \tag{69}$$

and keeping only the leading-order terms in $\hat{a}_1$ and $\hat{a}_2$, one finally gets

$$\hat{H} = \hat{P}_\phi\left(G_S\hat{a}_1 + G_{S_*}\frac{m_2}{m_1}\hat{a}_2\right) + \sqrt{A(1+\hat{P}_\phi^2 U_c^2)} \tag{70}$$

and the functions G_S and G_{S_*} read [26,28]

$$G_S = 2UU_c^2, \tag{71}$$

$$G_{S_*} = U_c^2\left[\frac{r_c\nabla\sqrt{A_{\rm eq}}}{1+\sqrt{Q}} + \frac{(1-\nabla r_c)\sqrt{A_{\rm eq}}}{\sqrt{Q}}\right], \tag{72}$$

where $A_{\rm eq}$ and $B_{\rm eq}$ are the Kerr potentials as defined in Eqs. (10) and (11) of Ref. [28], $\nabla \equiv (B_{\rm eq})^{-1/2}d/dr^{\rm EOB}$ is the proper radial gradient, and $Q \equiv 1 + \hat{P}_\phi^2 U_c^2$. Note that the U_c entering these two functions is given by Eq. (66) above, with the Kerr parameter $\hat{a}_0$ that is now given, at the same order, by

$$\hat{a}_0 = \hat{a}_1 + \frac{m_2}{m_1}\hat{a}_2 = \hat{a}_1 + \sigma, \tag{73}$$

where we recall that $\hat{a}_{1,2} = a_{1,2}/m_{1,2}$ [Eq. (60)] and $\sigma \equiv S_2/(m_1 m_2) = S_2/(M\mu)$, so that higher-order spin-spin couplings are also included in Eq. (70).

Restricting now to the simplest case (the Schwarzschild background, i.e., $\hat{a}_1 = 0$) and keeping only terms *linear* in σ (i.e., $U = U_c$), we obtain the following expression for the circular Hamiltonian of a spinning particle on a Schwarzschild background:

$$\hat{H} = G_{S_*}(U, \hat{P}_\phi)\hat{P}_\phi\sigma + \sqrt{A(U)(1+\hat{P}_\phi^2 U^2)}, \tag{74}$$

where the spin-orbit coupling function is still given by Eq. (72), but with $A_{\rm eq} = 1-2U$ and $B = A^{-1}$. Equation (74) constitutes the central piece of the Hamiltonian dynamics considered in this work.

Circular orbits are defined from the Hamiltonian in Eq. (74) in the standard way, demanding

$$\partial_U \hat{H}(U, \hat{P}_\phi; \sigma) = 0. \tag{75}$$

For a given U, this equation is solved to obtain the corresponding angular momentum $\hat{P}_\phi^{\rm circ}(U;\sigma)$. Then, from $\hat{P}_\phi^{\rm circ}(U;\sigma)$, one obtains

$$M\Omega \equiv \partial_{\hat{P}_\phi}\hat{H}(U, \hat{P}_\phi; \sigma)|_{\hat{P}_\phi^{\rm circ}}. \tag{76}$$

This is the way we construct the circular dynamics that feeds the Teukolsky equation and from which we compute the GW energy fluxes (see Sec. III A below). In the plots we label this numerically found CEO data as "HamNum" in

order to distinguish it from the linear-in-sigma analytical formulas derived below in Sec. III B (labeled as "HamAna").

The circular dynamics can be characterized in a gauge-invariant way in terms of the circular energy, the angular momentum, and the frequency parameter

$$x \equiv (M\Omega)^{2/3}, \tag{77}$$

which also allows us to compute $x(U)$ via Eq. (76). Plugging $\hat{P}_\phi^{\rm circ}(U;\sigma)$ into the Hamiltonian, Eq. (74), one gets $\hat{E}_{\rm circ}(x)$ when using the relation between U and x. In the case of a *nonspinning* particle on a Schwarzschild background, this procedure is fully analytic and yields the well-known expressions

$$\hat{E}_0 = \frac{1-2x}{\sqrt{1-3x}}, \tag{78}$$

$$\hat{P}_\phi^0 = \frac{1}{\sqrt{x(1-3x)}}. \tag{79}$$

When $\sigma \neq 0$, it is necessary to solve Eq. (75) numerically so that $\hat{E}^{\rm circ}(x)$ and $P_\phi^{\rm circ}(x)$ are obtained parametrically. Computing the energy and angular momentum curves along circular orbits, $\hat{E}^{\rm circ}(x,\sigma)$ and $\hat{P}_\phi^{\rm circ}(x,\sigma)$, or even the relation $\hat{E}^{\rm circ}(P_\phi^{\rm circ})$, is a useful tool to compare unambiguously the circular Hamiltonian dynamics with the dynamics obtained from the MP equations; see Sec. IV.

A. Numerical procedure for CEOs

The above descriptions might appear a bit complicated due to the choice to give a general discussion, but in fact it is easy to compute the CEO data. The starting point is Eq. (74), where we simply fix the EOB coordinates $(\hat{R},\phi)$ and the spin parameters $(\hat{a}_1,\sigma)$ as desired. It remains to find data for Ω and P_ϕ. To find the data for P_ϕ, we differentiate $\hat{H}$ with respect to U and demand that the resulting expression vanish [Eq. (75)]. In that expression we insert the orbital distance $\hat{R}$ and spin σ to make the right-hand side a function of P_ϕ only. This gives a condition to fix P_ϕ, which we solve numerically. Finally, $\partial_t\phi \equiv \Omega$ is obtained by differentiating $\hat{H}$ with respect to P_ϕ and inserting the values for $\hat{R}$ and P_ϕ. Thus, CEOs are given by the roots of two algebraic equations, which we solve using MATLAB's `fzero` routine. Before proceeding note that a given EOB radial coordinate is not trivially linked to a corresponding BL radial coordinate; see Secs. III D and III E.

B. Linear-in-σ energy and angular momentum

It is possible to obtain fully analytic expressions of the energy and angular momentum along circular orbits *if* we work consistently at linear order in σ. Such a result will be useful in various respects, e.g., in driving a comparison with the MP energetics and the HamNum energetics and to cross-check with other literature results obtained analytically from the MP at the quadrupolar order.

So, working now for a while at linear order in the spin, to determine $\hat{P}_\phi^{\rm circ}(U;\sigma)$, we pose $\hat{P}_\phi^{\rm circ}(U;\sigma) = \hat{P}_\varphi^0(U) + \sigma\hat{P}_\phi^1(U)$, where $\hat{P}_\phi^0$ is the solution of $\partial_U\hat{H}(U,\hat{P}_\phi;0)=0$ [i.e., Eq. (79) above with $x=U$] and we just need to solve for $\hat{P}_\phi^1$. From the definition of the orbital frequency $M\Omega \equiv \partial_{\hat{P}_\phi}\hat{H}(U,\hat{P}_\phi;\sigma)$ we can obtain x and the link between the inverse radial coordinate U and x along circular orbits,

$$U(x;\sigma) \equiv x + \frac{x^{5/2}}{1+\sqrt{\frac{1-2x}{1-3x}}}\sigma. \tag{80}$$

Using this relation, one finally finds the linear-in-σ expression of the angular momentum along circular orbits $\hat{P}_\phi^{\rm circ}(x;\sigma) \equiv \hat{P}_\phi^{\rm circ}(U(x;\sigma);\sigma)$, which reads explicitly

$$\hat{P}_\phi^{\rm circ}(x;\sigma) = \frac{1}{\sqrt{x(1-3x)}} - \left(1 - \frac{1-4x}{\sqrt{1-3x}}\right)\sigma, \tag{81}$$

and, by inserting the two equations above into Eq. (74), the corresponding expression for the energy reads

$$\hat{E}^{\rm circ}(x;\sigma) = \frac{1-2x}{\sqrt{1-3x}} - \frac{x^{5/2}}{\sqrt{1-3x}}\sigma, \tag{82}$$

which manifestly contains the nonspinning particle limit; see Eq. (78). These two relations fully characterize the circular orbits of a spinning particle on a Schwarzschild BH at linear order in the spin. We will use these in Sec. IV to perform comparisons with the corresponding energetics obtained numerically from the Hamiltonian as well as with the energetics from the MP equations.

C. The spin-induced ISCO shift

The ISCO location and the corresponding minimal angular momentum are defined by the two equations

$$\begin{aligned}\partial_U\hat{H}(U_{\rm ISCO},\hat{P}_\phi^{\rm ISCO};\sigma)&=0,\\ \partial_U^2\hat{H}(U_{\rm ISCO},\hat{P}_\phi^{\rm ISCO};\sigma)&=0.\end{aligned} \tag{83}$$

This system can be solved numerically to obtain $(U_{\rm ISCO},\hat{P}_\phi^{\rm ISCO})$ and eventually this yields the ISCO frequency parameter $x_{\rm ISCO}^{\rm HamNum}$ that we list in the sixth column of Table II.

As we did above, it is also instructive to solve this system analytically working at linear order in σ. We obtain

TABLE II. Frequency parameter x at the ISCO of a spinning particle on a Schwarzschild background computed with different dynamics. Entries with a backslash / mean that the ISCO values for these configurations could not be found; see text.

σ	$x^{\rm T}_{\rm ISCO}$	$x^{\rm P}_{\rm ISCO}$	$x^{\rm OKS}_{\rm ISCO}$	$x^{\rm HamAna}_{\rm ISCO}$	$x^{\rm HamNum}_{\rm ISCO}$	$x^{\rm BFG}_{\rm ISCO}$
0.90	0.222448	0.231253	/	0.197290	0.201378	0.201040
0.70	0.203471	0.204538	/	0.190480	0.193037	0.192750
0.50	0.189398	0.189541	0.196051	0.183680	0.185012	0.184830
0.30	0.178680	0.178692	0.179119	0.176870	0.177361	0.177290
0.10	0.170248	0.170248	0.170257	0.170070	0.170123	0.170120
−0.10	0.163426	0.163426	0.163420	0.163260	0.163319	0.163310
−0.30	0.157786	0.157790	0.157670	0.156460	0.156951	0.156880
−0.50	0.153042	0.153066	0.152642	0.149660	0.151010	0.150810
−0.70	0.149000	0.149076	0.148144	0.142850	0.145476	0.145120
−0.90	0.145521	0.145696	0.144062	0.136050	0.140326	0.139800

$$U^{\rm ISCO} = \frac{1}{6} + \sigma \frac{1}{18\sqrt{2}}, \tag{84}$$

$$\hat{P}^{\rm ISCO}_{\phi} = \pm 2\sqrt{3} + \sigma\left(\frac{\sqrt{2}}{3} - 1\right). \tag{85}$$

Using the inversion of the link between x and U in Eq. (80),

$$x(U) = U - \frac{U^{5/2}}{1 + \sqrt{\frac{1-2U}{1-3U}}}\sigma, \tag{86}$$

we also obtain

$$x^{\rm ISCO} = \frac{1}{6} + \frac{\sigma}{12\sqrt{6}} \tag{87}$$

for the ISCO frequency parameter. Note that below we will write Eq. (87) as $x^{\rm ISCO}_{\rm HamAna}$ to distinguish it from the numerical solution of Eq. (83). The ISCO energy is

$$\hat{E}^{\rm ISCO} = \frac{2\sqrt{2}}{3} - \frac{\sqrt{3}}{108}\sigma. \tag{88}$$

These results [specifically, Eqs. (85), (87), and (88)] coincide with the corresponding linear-in-spin expressions obtained analytically by Bini, Faye, and Geralico [30] starting directly from the MP. For completeness, we quote also their expression for $x_{\rm ISCO}$, which also includes the σ^2 term and reads

$$x^{\rm BFG}_{\rm ISCO} = \frac{1}{6} + \frac{\sigma}{12\sqrt{6}} + \frac{\sigma^2}{216}. \tag{89}$$

Thus, our linear-in-σ calculation gives a useful consistency check that the circular dynamics of Ref. [30] is precisely the same as the one provided by the limit of the EOB Hamiltonian. This finding will turn out to be useful below to obtain a linear-in-σ link between the EOB and the BL radial coordinates along circular orbits.

D. Relation between the EOB and Schwarzschild radial coordinates

For our application of the dynamics to the Teukolsky equation it is necessary to have an explicit connection between the EOB and the Schwarzschild radial coordinates, or equivalently their inverses $U = M/r^{\rm EOB}$ and $u = M/r$, at least at linear order in σ. For a *nonspinning* particle, we would just have $u = U$. For a *spinning* particle, however, this relation will be corrected by a term linear in sigma. This relation does not seem to exist in the literature. Here we shall derive it in the simplifying case of circular orbits.

An easy way to relate u with U is to equate the two functions $x(u)$ and $x(U)$, as obtained from the MP using a given SSC on the one hand and from the Hamiltonian on the other hand. The relation $x(U)$ was already given in Eq. (86). Similarly, from the MP with the T SSC, one obtains at linear order in σ

$$x(u) = u - u^{\frac{5}{2}}\sigma, \tag{90}$$

which follows when linearizing Eq. (22) of Paper I or Eq. (4.26) of Ref. [40]. Equating the two expressions for the frequency parameter, we thus find

$$u = U + \frac{\sqrt{\frac{1-2U}{1-3U}}}{1 + \sqrt{\frac{1-2U}{1-3U}}}U^{5/2}\sigma, \tag{91}$$

and correspondingly

$$\hat{r} = \hat{R} - \frac{1}{\hat{R}\sqrt{1 - \frac{3}{\hat{R}}}}\sigma. \tag{92}$$

Of course, these results can also be applied to determine the ISCO shift of the BL radius. From Eq. (84) one obtains the σ-dependent ISCO shift in EOB coordinates

$$\hat{R}^{\rm ISCO} = 6 - \sqrt{2}\sigma, \tag{93}$$

and from Eq. (92) we get

$$\hat{r}^{\rm ISCO} = 6 - \frac{2}{3}\sqrt{6}\sigma, \tag{94}$$

consistently with the corresponding correction in Ref. [30]; see Eqs. (4.38)–(4.40) there.

E. Orbital dynamics for the Teukolsky equation source term

The particle source term of the Teukolsky equation is assembled from the variables (1). Thus we cannot directly use the natural variables of the EOB Hamiltonian formalism: we have to process them further. First, we calculate the BL coordinates and their time derivatives from the EOB ones. While the angular coordinates are the same, the BL radius is computed from the ansatz made in Sec. III D, i.e., at linear order in σ we assume $x(u) = x(U)$. As a matter of choice, in the code the resulting equation

$$u - u^{5/2}\sigma = U - \frac{U^{5/2}}{1 + \sqrt{\frac{1-2U}{1-3U}}}\sigma \tag{95}$$

has been solved numerically for u, instead of using the strict analytical linear-in-σ solution (92). We have checked that the results are essentially the same; e.g., for $\sigma = 0.9$ and over the interval $R \in (5, 30)$ the solutions for r differ at most by 0.5%. Due to the linear-in-σ approximations used, there is anyway a small uncertainty in the interpretation of the Hamiltonian CEO dynamics in terms of r. This is one reason why we prefer to discuss the results in terms of gauge-invariant parameters like the frequency whenever possible. Continuing to process the EOB variables, the tangent vector can be computed from the coordinate velocities using

$$v^i = \frac{dX^i}{dt} v^t, \tag{96}$$

where we compute v^t according to Eq. (30). To compute p_μ and $S^{\mu\nu}$, we need to impose again a SSC. For simplicity we choose here the linearized T SSC [Eq. (16)]. Recall that at linear order the T SSC is equivalent to the P SSC and we have

$$p_\mu = \mu v_\mu, \tag{97}$$

which directly relates the kinematical momenta to the four-velocity. The spin tensor $S^{\mu\nu}$ is computed according to Eq. (35), with $V^\mu = v^\mu$. The time derivatives are computed numerically, but for CEOs they are found to vanish anyway. As a side remark, note that the EOB momenta that are evolved by the Hamiltonian EOM are not used at all to compute the variables (1).

IV. ENERGETICS AND THE ISCO SHIFT

In this next section we want to analyze the different circular dynamics that we have produced using the respective approaches described above. We discuss the energetics and how the shift of the ISCO due to the particle's spin changes between the various cases. In the analysis of the different prescriptions we pick the Hamiltonian case as the reference solution. This does not imply that the Hamiltonian description would be more correct than the others; it is only motivated by our research agenda, i.e., we plan to use our findings for the EOB Hamiltonian case to model waveforms.

A. Energetics of circular orbits

To drive gauge-invariant comparisons of the dynamics, one may analyze the binding energy as a function of the angular momentum, as in, e.g., Ref. [46]. Alternatively, as done here, one can consider the binding energy as a function of the orbital frequency Ω, or of the frequency parameter x. Note that at a given BL r the orbital frequency Ω differs between the respective dynamics, and thus x does as well.

The energetics are represented via the reduced binding energy function

$$e_\sigma(x) \coloneqq \hat{E}(x, \sigma) - 1, \tag{98}$$

where $\hat{E}(x, \sigma)$ is the mass-reduced energy constant on a circular orbit; see Eqs. (37), (82), and (B1), respectively. From $e_\sigma(x)$ we seek to isolate i) the contribution due to the body's spin and, in particular, ii) the spin-orbit (SO) contribution.[1] For i) we simply compare the energetics with the nonspinning particle limit, i.e., we consider the fractional differences

$$1 - \frac{e_\sigma}{e_0}. \tag{99}$$

For ii) we note that from the SO Hamiltonian (69) an ansatz for the energy function can be motivated in the Newtonian limit, i.e., at low frequencies, which reads

$$\hat{E}(x, \sigma) = \hat{E}_0(x) + h^{\rm lin}_{\rm SO}(x)\sigma + \mathcal{O}(\sigma^2), \tag{100}$$

where the first term corresponds to the nonspinning dynamics and the second term to the SO interaction at linear order in σ. The $\mathcal{O}(\sigma^2)$ terms describe either high-order SO contributions or spin-spin self-interactions. By construction, the Hamiltonian dynamics does not contain $\mathcal{O}(\sigma^2)$ terms, so $h^{\rm lin}_{\rm SO}(x)$ is analytical and can be read off from Eq. (82). From the MP dynamics we extract the SO contribution according to

[1] A similar analysis has been applied to study the spin-orbit interaction in numerical relativity simulations of neutron star mergers [47].

$$e_{\rm SO}(x,|\sigma|) \coloneqq \frac{1}{2\sigma}(\hat{E}(x,+|\sigma|) - \hat{E}(x,-|\sigma|)). \qquad (101)$$

This formula is obviously insensitive to the sign of the spin because it employs pairs of data sets with spins of the same magnitude $|\sigma|$ but opposite sign. Note that $e_{\rm SO}(x,\sigma)$ computed as above depends on σ if the *additive* ansatz (100) does not hold, i.e., presumably at high frequencies and at high spins. Thus, in general we expect that $e_{\rm SO} = e_{\rm SO}(x,\sigma)$, while for fully linear-in-spin expressions like the HamAna formula (82) the quantity $e_{\rm SO}$ is actually spin independent, $e_{\rm SO} = e_{\rm SO}(x,0)$.

Let us now compare these quantities for the different dynamics. First, the full energy curves $e_\sigma(x)$ are shown for seven representative values of the spin $\sigma \in (0, \pm 0.2, \pm 0.5, \pm 0.9)$ in the left panel of Fig. 1, illustrating the system's energetics along circular orbits from large distances (low frequencies) to small distances (high frequencies) close to the ISCO, and in some cases even beyond. The black dot markers refer to the value of $e_\sigma(x)$ at $x = x_{\rm ISCO}$ as computed by Eq. (87). The figure includes lines for the T SSC, the P SSC, and the OKS SSC, as well as for the Hamiltonian formalism. Note that the Hamiltonian formalism actually provides two results, namely, the analytic approximation ("HamAna") [Eq. (82)] and the full numerical solution of Eqs. (75) and (76) inserted into Eq. (74) ("HamNum"). The comparison of these two is an important corollary result for understanding the character of the EOB Hamiltonian though this is not explored in detail here.

Looking at the panels, at first sight the energetics of the three MP dynamics are qualitatively comparable with one another and with the Hamiltonian counterpart. While at small x the curves are visually on top of each other (see inset), one clearly observes that the spin interactions become more significant as x increases (smaller orbital radii) *and* as $|\sigma|$ increases. Towards the ISCOs the analytic formula for the energy, Eq. (82), shows significant differences with respect to the one from the MP dynamics. In general, in the regime of large frequencies, $x \gtrsim 0.1$, positive spins (i.e., spins aligned with the orbital angular momentum) involve the worst mutual agreement between the curves; among the various cases the OKS SSC shows the least consistency with the Hamiltonian reference case for large positive spins. By contrast, the numerical solution of the Hamiltonian dynamics is in visual agreement with the analytical approximation over the whole spin and frequency range considered. Interestingly, the T SSC and the P SSC are also mutually consistent.

Let us now compare the energetics with the *nonspinning* particle limit. The right panel of Fig. 1 shows the fractional spin contribution, i.e., Eq. (99), up to $x^{\rm HamAna}_{\rm ISCO}$. For small spin magnitudes $\sigma = \pm 0.2$ all dynamical prescriptions are in perfect agreement over the whole frequency range considered. The relative differences with respect to the nonspinning limit are small, namely $\lesssim 5\%$. Of course, for larger spin magnitudes the energetics deviate much more from the nonspinning limit; in general, we observe that at a given spin magnitude positive spins entail a larger deviation from the nonspinning limit than negative spins, e.g., for $|\sigma| = 0.9$ the differences close to the ISCO are $\sim 50\%$ for $\sigma = 0.9$ while they are $\sim 15\%$ for $\sigma = -0.9$. For large spin

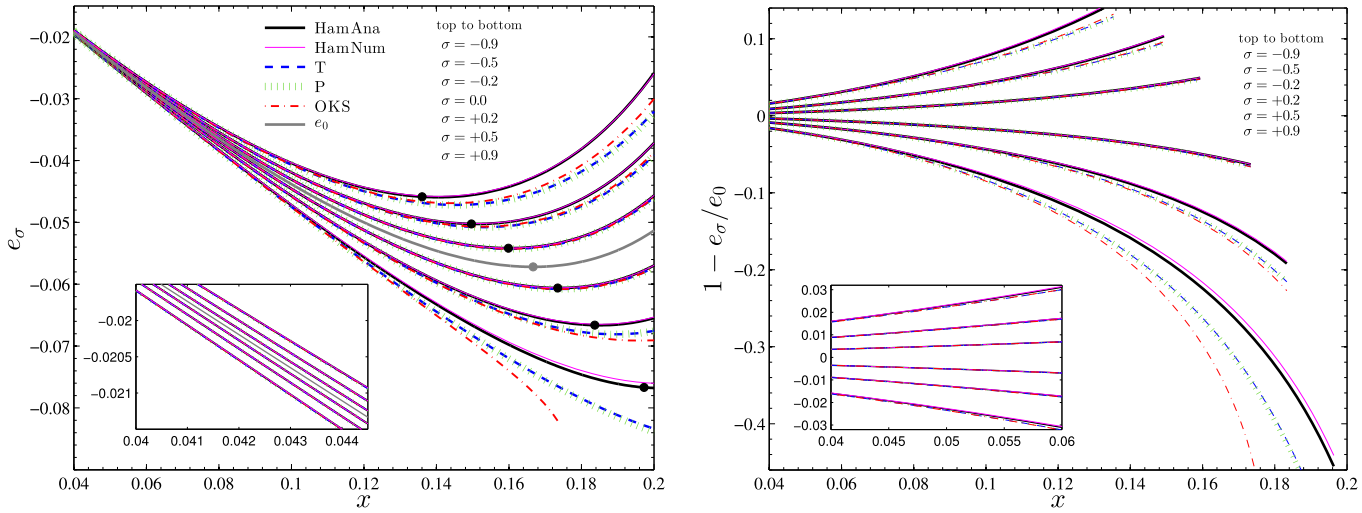

FIG. 1. Analysis of spin effects on the energetics of circular orbits. Left panel: Contrasting the binding energy $e_\sigma(x) \equiv \hat{E}_\sigma(x) - 1$ for different values of the particle spin σ as obtained on the one hand analytically (solid black) at linear order in the spin from Hamiltonian dynamics, i.e., using $\hat{E}^{\rm circ}_\sigma(x)$ of Eq. (82), and on the other hand numerically from the Hamiltonian (solid magenta), from the MP with the T SSC (blue dashed), the P SSC (green dotted), and the OKS SSC (red dash-dotted), respectively. The filled black markers are the analytic energy values at the analytic ISCO frequencies, obtained from $\hat{E}^{\rm circ}_\sigma(x^{\rm HamAna}_{\rm ISCO})$. Right panel: The (fractional) spin contributions [see Eq. (99)], shown up to $x^{\rm HamAna}_{\rm ISCO}$ [see Eq. (87)].

magnitudes the energetics of the different prescriptions are still in agreement at small frequencies (see inset) but again show significant variations at large frequencies, $x \gtrsim 0.1$. Furthermore, note that this plot highlights the repulsive character of the spin interactions for $\sigma > 0$ (spin aligned to orbital angular momentum) and the attractive character for $\sigma < 0$ (spin antialigned to orbital angular momentum).

Next, the SO contribution is analyzed in Fig. 2, which shows $e_{\rm SO}(x,\sigma)$ as computed by Eq. (101) for the three MP dynamics (T, P, OKS) and the numerical solution of the Hamiltonian dynamics (HamNum). These curves are contrasted with the analytical term $e_{\rm SO}^{\rm HamAna} = h_{\rm SO}^{\rm lin}$, as read off from Eq. (82) (HamAna). From left to right the panels of Fig. 2 refer to the representative spin values $|\sigma| \in (0.2, 0.5, 0.9)$. The panels show that the SO interaction is modeled in a qualitatively compatible way in all the different cases; only for large frequencies and for $|\sigma| = 0.9$ the OKS SSC entails a drastic inconsistency in the SO part compared with the other approaches. Looking at this figure, it is striking that in all three panels the P SSC and the T SSC behave visually equivalently in mutual comparison. The bottom panels show the relative differences with respect to the linear-in-sigma analytic formula, $|\Delta e_{\rm SO}| = |1 - e_{\rm SO}^{\rm X}/h_{\rm SO}^{\rm lin}|$. The relative differences of the P and the T SSCs to the Hamiltonian dynamics grow from only 0.001% (at $x \sim 0.04$) to 0.01% (at $x \sim x_{\rm ISCO}$) for $|\sigma| = 0.2$. For $|\sigma| = 0.9$ the differences increase by approximately 1 order of magnitude, which amounts to a difference of $\lesssim$1% close to the ISCO. These differences are likely due to nonlinear-in-spin terms included in the MP dynamics when using the T and P SSCs, which are invalidating the linear-in-spin ansatz of the Hamiltonian approach; see Eq. (100). The SO interaction observed for the MP OKS dynamics instead shows more significant differences with respect to both the T and the P SSC as well as to the Hamiltonian reference. Focusing on small spins, $|\sigma| \sim 0.2$, and "large" separations $x \sim 0.04$, the OKS case already manifests a SO contribution that is rather inconsistent with the others. The relative differences to the Hamiltonian case are in general 1 order larger than those observed for the T and P SSCs. At $|\sigma| = 0.9$ the deviations become visually apparent; in particular, at high frequencies the divergence becomes most prominent. This disagreement is at first sight surprising from the point of view that the OKS SSC EOM are linear in spin, as is the HamAna expression. However, though the EOM are linear in spin for the OKS SSC, its energy dependency on the spin appears to be not necessarily linear in spin, which explains why the SO part can be i) spin dependent, and ii) different from the Hamiltonian analytical formulas. Furthermore, a disagreement with the Hamiltonian case is reasonable because the Hamiltonian comes from a by-hand linearization of the T/P MP in spin, whereas the OKS SSC stems from the idea of choosing an observer such that the MP are linear in spin. Thus, the Hamiltonian is dynamically closer to the T/P MP, while the OKS formalism comes from another, independent approach.

B. ISCO results

Besides comparing the energetics, the differences in the dynamics can be analyzed in terms of the spin-dependent shift of the ISCO location; see Appendix A for a reminder of the notion of the ISCO for a *nonspinning* particle. We report in Table II the values of $x_{\rm ISCO}$ for the different dynamical prescriptions and the different approximations: the MP with the T SSC, the P SSC, and the OKS SSC, and the Hamiltonian dynamics, either in the form of the analytic linear-in-spin expression (87), or in the full numerical

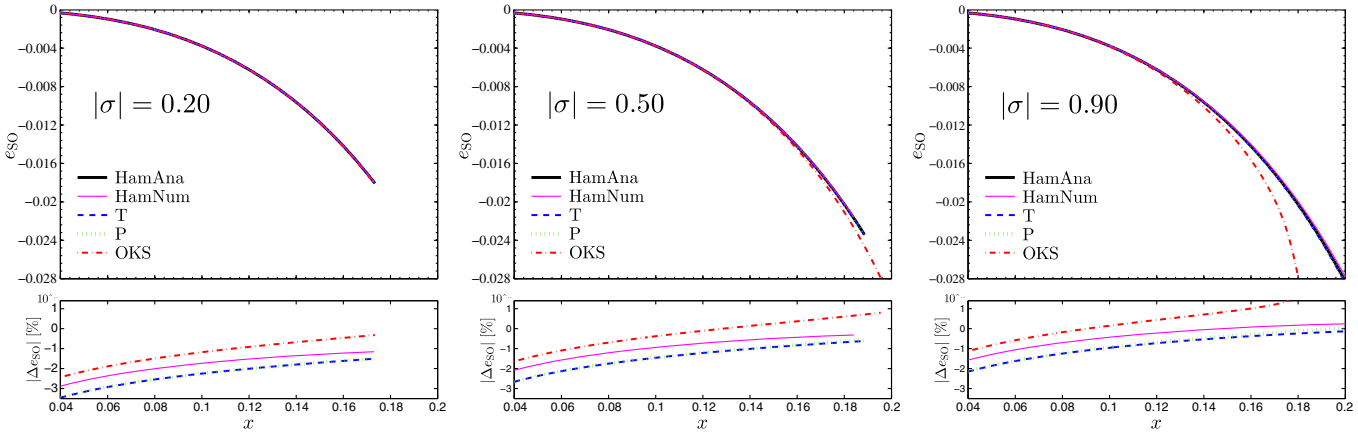

FIG. 2. Analysis of the spin-orbit contribution, $e_{\rm SO}$, to the energetics of circular orbits. Top panels: Comparing the analytic formula for the spin-orbit contribution in the Hamiltonian case (HamAna), as read off from Eq. (82), with $e_{\rm SO}(x,\sigma)$ for the different dynamical prescriptions, computed using Eq. (101). From left to right the panels show three representative values of the spin: $|\sigma| = 0.2, 0.5, 0.9$. Bottom panels: Relative differences of the SSC curves with respect to the Hamiltonian curves, $|\Delta e_{\rm SO}| = |1 - e_{\rm SO}^{\rm X}/e_{\rm SO}^{\rm HamAna}|$, where X refers to the HamNum, T, P, and OKS cases, respectively. Note that the vertical scale is logarithmic here.

solution of Eq. (83). Additionally, we include the quadrupolar result as derived by Bini, Faye, and Geralico in Ref. [30] (BFG hereafter). We stress that, for the OKS SSC, ISCOs could not be found at spins $\sigma \gtrsim 0.52$. Similarly the ISCO frequency diverges for the P SSC at spins $\sigma \gtrsim 0.94$. Among the considered MP options, only the T SSC gives well-defined ISCOs for every $\sigma \in [-1, +1]$ (and, in fact, even beyond that interval).

Browsing through Table II, one observes that the T and P SSCs behave similarly; the ISCO values for the frequency parameter agree in all cases in the first two significant digits, except for the highest spin value $\sigma = 0.9$. A slightly worse agreement is seen between the numerical Hamiltonian approach (HamNum) and the linear-in-sigma analytic formula (HamAna). While the ISCO frequencies also share the same first two significant digits for small spins $|\sigma| \leq 0.3$, they deviate more strongly for larger values of the spin magnitude. These consistencies between the T and P SSCs on the one hand and HamNum and HamAna on the other hand were already apparent in the analysis of the energetics made in the previous section and are confirmed here. Surprisingly, we also observe strong agreement (two digits) between $x_{\rm ISCO}^{\rm HamNum}$ and $x_{\rm ISCO}^{\rm BFG}$, i.e., the quadrupolar result of Ref. [30]. This result suggests that the Hamiltonian implicitly models higher-order spin terms connected to the spin-induced quadrupole of the body.

Table II is complemented by Fig. 3, which shows in the top panel the ISCO shift

$$\begin{aligned}\Delta x_{\rm ISCO}(\sigma) &= x_{\rm ISCO}(\sigma) - x_{\rm ISCO}(0) \\ &= x_{\rm ISCO}(\sigma) - \frac{1}{6} \end{aligned} \tag{102}$$

due to the particle's spin. For small spins $|\sigma| \lesssim 0.2$ all the different cases are in agreement with one another, as expected. The agreement between the T and P SSCs is striking over the whole range of σ, though it deteriorates a bit for large positive spins where the ISCO for the P SSC is divergent. For negative σ the OKS SSC also seems compatible with the other two. For large positive spin magnitudes the plot clearly shows the divergence of the ISCO within the OKS and P SSCs. Confirming the impression of Table II, the numerically found ISCOs of the Hamiltonian dynamics are very close to the BFG formula, which includes the quadrupolar contributions, over the whole spin range. This is an interesting but rather surprising numerical coincidence, with σ^2 terms that are effectively present in the numerical solution. The bottom panel shows the differences with respect to the linear-in-sigma analytical formula (87). For moderate spins $|\sigma| \lesssim 0.2$ the ISCO frequencies of the different dynamics differ by at most ∼20% from the linear-in-sigma Hamiltonian expression. As expected, the numerical and analytical Hamiltonian solutions for the ISCO are quite compatible,

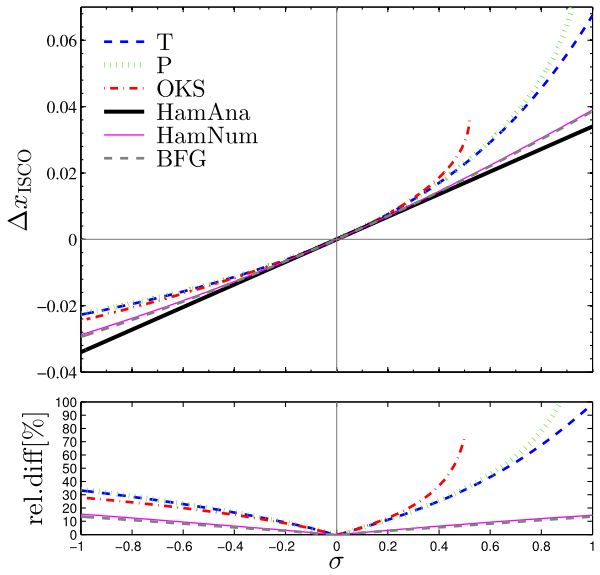

FIG. 3. Top panel: Shift of the ISCO frequency parameter due to the particle's spin, $\Delta x_{\rm ISCO} = x_{\rm ISCO} - 1/6 = (M\Omega_{\rm ISCO})^{\frac{2}{3}} - 1/6$. Bottom panel: Relative differences of the ISCO shifts $\Delta x_{\rm ISCO}$ with respect to the linear-in-sigma analytical formula of the Hamiltonian dynamics (HamAna). For the OKS SSC (red, dash-dotted) the ISCO computations fail for spins $\sigma > 0.52$ (see discussion in text); for the P SSC (green, dashed) the ISCO computations fail for spins $\sigma > 0.94$. In general, the figure illustrates how all prescriptions converge to the same ISCO frequency as $\sigma \to 0$. At large values of σ the ISCO frequencies are drastically different between the various dynamical formalisms. In particular, we observe that the ISCOs obtained from the Hamiltonian analytically (HamAna) and fully numerically (HamNum) agree well with one another ($\lesssim$15%), as well as with the quadrupolar result of Ref. [30] (BFG, gray dashed). For spins $\sigma < 0.2$ the ISCO frequencies of the T, P, and OKS SSCs are also very compatible with one another.

with only ∼15% deviation at maximum. Also the BFG result agrees with the HamAna result at that level.

As a side note we mention that, when taking the viewpoint that a SSC is just a gauge choice within the pole-dipole approximation, one would not expect such discrepancies between the curves of the three SSCs in Fig. 3 because $x_{\rm ISCO}$ is a gauge-invariant quantity. One can argue that our plots are missing parallel shifts of the curves along the σ axis, since the reference point according to which we define σ depends on the SSC, but even such shifts could not make the curves match each other. Thus, our results indicate that the different choices of a centroid made in the different dynamical approaches of the pole-dipole approximation actually lead to different physical descriptions, rather than only artificial gauge effects. Note, however, that if all the multipole moments of the test body were present, i.e., we did not have just a pole-dipole approximation, then a SSC would be just a gauge choice; see Ref. [48] for more details on this issue.

V. ASYMPTOTIC GW FLUXES

We now compare the GW fluxes produced by the different circular dynamics of the spinning particle discussed in Secs. II and III. We briefly explain the numerical algorithm employed in TEUKODE for computing the waveforms; more details can be found in Paper I. For an overview of the existing literature on the topic of GWs from a spinning particle, see Refs. [36,38,49–52].

A. Waveform generation algorithm

We compute the GW fluxes associated with the different circular dynamics using the waveform generation algorithm developed in Refs. [29,53–56]. The latter approach is based on solving the Teukolsky equation (TE) [57,58] in $(2+1)$ dimensions on hyperboloidal slices of the Kerr spacetime [59–63], and including the pole-dipole particle source term. Here we briefly summarize the main features of the method, referring to our previous work for details on numerical convergence and thorough cross-checks with literature results in the nonspinning test-particle limit [64–70].

The TE is formulated using horizon-penetrating and hyperboloidal coordinates following Zenginoğlu's scri-fixing approach [60–62]. This technique allows us to measure the GW signal at future null infinity (scri), where it is unambiguously defined. This approach is advantageous for numerical treatments because (i) the horizon and scri are included in the computational domain, and (ii) outgoing (ingoing) radial coordinate light speeds vanish at the horizon (at scri), so no boundary conditions are needed. The particular coordinates employed here are the HH_{10} coordinates introduced in Ref. [56]; see also Ref. [71]. The $(3+1)$-dimensional TE in these coordinates is then decomposed to exploit the axisymmetry of the background by separating each Fourier m mode in the azimuthal direction. This results in $(2+1)$-dimensional wave-like equations for each m mode of the radius rescaled Weyl scalar, $r\Psi_4$. From the Weyl scalar we reconstruct the multipoles h_m of the metric waveform and then decompose it into spin-weighted spherical harmonics $h_{\ell m}$ [56].

Numerical solutions of the TE in the time domain are obtained using TEUKODE, a computer code specifically designed for particle perturbations of a rotating BH [29,55,56,72]. The TE is written as a first-order-in-time and second-order-in-space system and discretized in time using the method of lines. The spatial two-dimensional domain is represented by a uniform mesh $(y,\theta) \in [y_{\mathrm{horizon}}, y_{\mathrm{scri}}] \times (0,\pi)$, where y is the radial HH_{10} coordinate, with $N_y \times N_\theta$ grid points. Finite differencing approximations are used for the spatial derivatives. In this work we have used sixth-order finite-differencing stencils and employed a resolution of $N_y \times N_\theta = 4800 \times 400$.

To assess the accuracy of our numerical results, we compared in Paper I our fluxes for the nonspinning particle case against the highly accurate reference solutions of Hughes, which were computed using an improved version of the frequency-domain code appearing in Refs. [68,69,73]. Assuming that the spin of the particle does not significantly decrease the numerical accuracy, we estimated our relative numerical accuracy level at ~0.2–0.5%, depending on whether the full flux or a dominant multipole, or a subdominant multipole, is considered. The same accuracy estimate holds for the present study. We mention that the results for the T SSC were already published in Paper I, where we had employed a higher resolution of 6000×500 points for the outermost orbits at $r = 30M$ in order to have increased accuracy in the weak field. In the current study we have, however, used 4800×400 points all over. So the $r = 30M$ T SSC results are a bit more accurate than the other results presented here.

B. Results

We computed the fluxes for each of the four dynamics at various BL radii, usually $r/M \in \{4, 5, 6, 8, 10, 12, 20, 30\}$, and for the four particle spins $\sigma = \pm 0.5, \pm 0.9$. The multipolar GW fluxes read

$$F = \sum_{m=1}^{\infty} F_m = \sum_{\ell=2}^{\infty} \sum_{m=1}^{m=\ell} F_{\ell m} = \frac{2}{16\pi} \sum_{\ell=2}^{\infty} \sum_{m=1}^{m=\ell} (m\Omega)^2 |r h_{\ell m}|^2, \quad (103)$$

where we follow the notation of Ref. [74]. Note that F_m and $F_{\ell m}$ are defined to contain both the m and $-m$ contributions, which are equivalent for GWs from a particle on CEOs. GW fluxes are typically studied as functions of the frequency parameter x; see Eq. (77). Furthermore, it is convenient to use the normalization

$$\hat{F}_{\ell m}(x,\sigma) = \frac{F_{\ell m}(x,\sigma)}{F^{\mathrm{LO}}_{\ell m}(x)}, \quad (104)$$

where $F^{\mathrm{LO}}_{\ell m}(x)$ is the leading-order (LO) flux predicted by the quadrupole formula. Our waveform algorithm directly provides the fluxes F_m with all ℓ contributions included; $F_{\ell m}$ is computed from the projected metric multipoles $h_{\ell m}$. We further define

$$\hat{F}_m = \begin{cases} \frac{F_m}{F^{\mathrm{LO}}_{2m}} & m = 1 \\ \frac{F_m}{F^{\mathrm{LO}}_{mm}} & \text{otherwise} \end{cases} \quad (105)$$

in order to present LO-normalized m-mode fluxes.

For each dynamics we have computed the fluxes for the modes $m = 1, 2, 3$. The $\hat{F}_m$ are reported in Table V and Table VI for $m = 1, 2$ and $m = 3$, respectively. The results

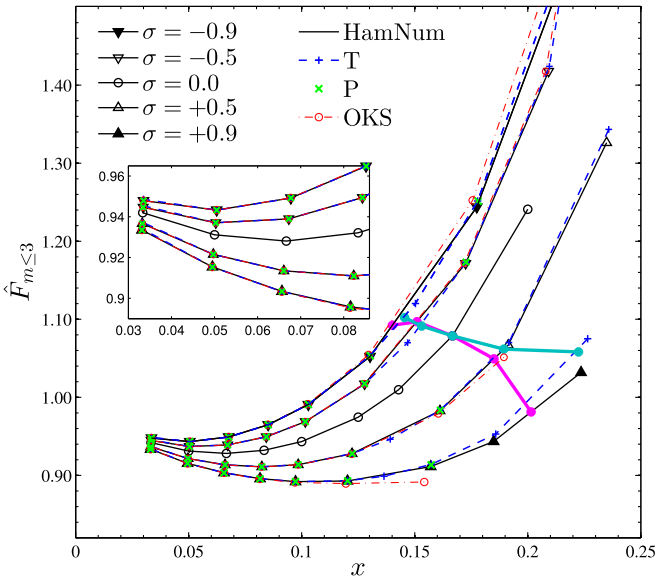

FIG. 4. Comparison of the full GW energy flux, approximated by the sum of the $m = 1$, 2, 3 modes, containing all ℓ contributions, over the variable $x = (M\Omega)^{2/3}$, where Ω is the particle's orbital frequency. We contrast four different circular dynamics of a spinning particle around a Schwarzschild BH: Hamiltonian dynamics (solid black, triangles), Mathisson-Papapetrou dynamics with the T SSC (blue dashed, pluses), the P SSC (green crosses), and the OKS SSC (red dash-dotted, circles). We consider the four spin values $\sigma = -0.9, -0.5$, 0.5, 0.9, and the nonspinning particle limit (solid black, circles). Additionally, the fluxes at the ISCOs are connected along the different spins for the Hamiltonian case (thick magenta) and the T case (thick cyan).

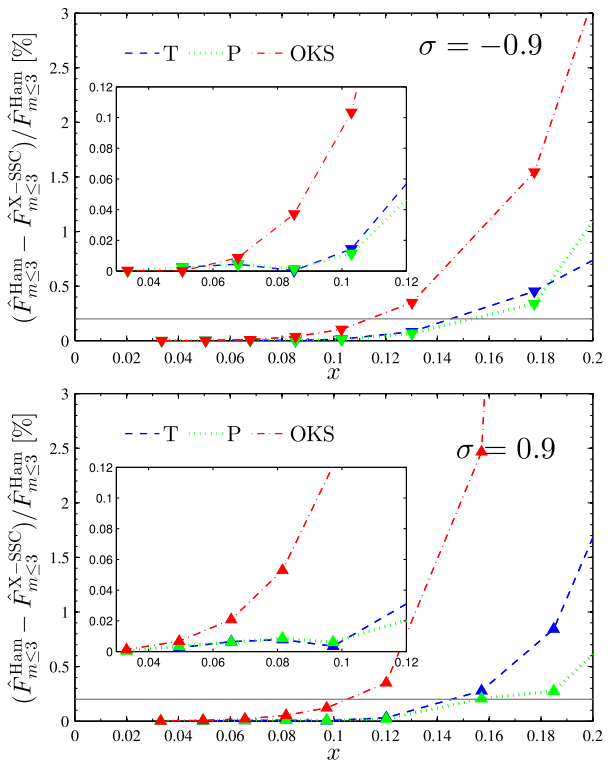

FIG. 5. Relative differences in the full GW flux, approximated as the sum over the $m = 1, 2, 3$ modes, produced using the T SSC (blue, dashed), the P SSC (green, dotted), and the OKS SSC (red, dash-dotted) with respect to the Hamiltonian reference case. We consider the two dimensionless particle spins $\sigma = -0.9$ (top panel) and $\sigma = 0.9$ (bottom panel). The gray horizontal lines at 0.2% mark our estimated relative numerical accuracy. The figures show that the GW fluxes of the various dynamics agree with one another at the level of our accuracy up to $x \lesssim 0.11$ ($r \gtrsim 10M$). At smaller radii the agreement is still at the ∼1% level almost up to $r = 5M$, except for positive spins with the OKS SSC. In this sense the OKS SSC shows a different strong-field behavior than the other tested SSCs.

are illustrated in Fig. 4, which reports the total normalized fluxes, i.e., the *sum* of the $\hat{F}_m$ (see Fig. 6 for the separate m-mode fluxes). The fluxes from the Hamiltonian dynamics are shown in solid black, with upward and downward triangles distinguishing the different σ. The fluxes from the T SSC are shown as small blue pluses, connected by a thin, dashed line. The fluxes from the P SSC are not connected by lines, but rather represented by green crosses. Finally, the fluxes for the OKS SSC are shown as red dash-dotted lines with empty circles. For the Hamiltonian case and for the T SSC, we have additionally included lines that connect the interpolated fluxes at the ISCOs for the five different spins (magenta for Hamiltonian ISCOs and cyan for T SSC ISCOs). These ISCO lines are omitted for the OKS and P SSCs. The data for the nonspinning case, shown as black open circles connected by a solid line, were computed by Hughes in the frequency domain at very high accuracy and kindly made available to us; see Refs. [68,69,73,75]. The differences between the various fluxes with respect to the fluxes from the Hamiltonian dynamics are shown in Fig. 5 for $\sigma = \pm 0.9$.

The figures show that for all σ values and up to $x \lesssim 0.12 - 0.16$ ($r \gtrsim 10 - 8M$) all the fluxes agree with the Hamiltonian case within our numerical accuracy (∼0.2%). Notably, for $x \lesssim 0.04$ ($r \gtrsim 20M$) the relative differences are at the level of ∼0.02% in all cases tested. For the negative spins $\sigma = -0.9$ and $\sigma = -0.5$, the flux differences remain at the ∼1% level even beyond the T SSC ISCOs at $x_{\rm ISCO} \approx 0.146$ and $x_{\rm ISCO} \approx 0.153$, respectively. For positive spins $\sigma = +0.5$ and $\sigma = +0.9$ the agreement is slightly worse, and in particular the OKS case exhibits a systematic deviation for $x \gtrsim 0.12$. We note that our assumption on the coordinate transformation from the EOB to the BL radial coordinate might contribute to differences seen in the fluxes (91) (because the BL r enters the source term of the TE).

In conclusion, the differences in the fluxes for $x \gtrsim 0.1$ are consistent with our analysis of the dynamics' energetics in Sec. IV. The present analysis of the fluxes constitutes a further means to probe the fact that the different dynamical prescriptions are not completely equivalent at large frequencies and large spins. Additionally, the computation

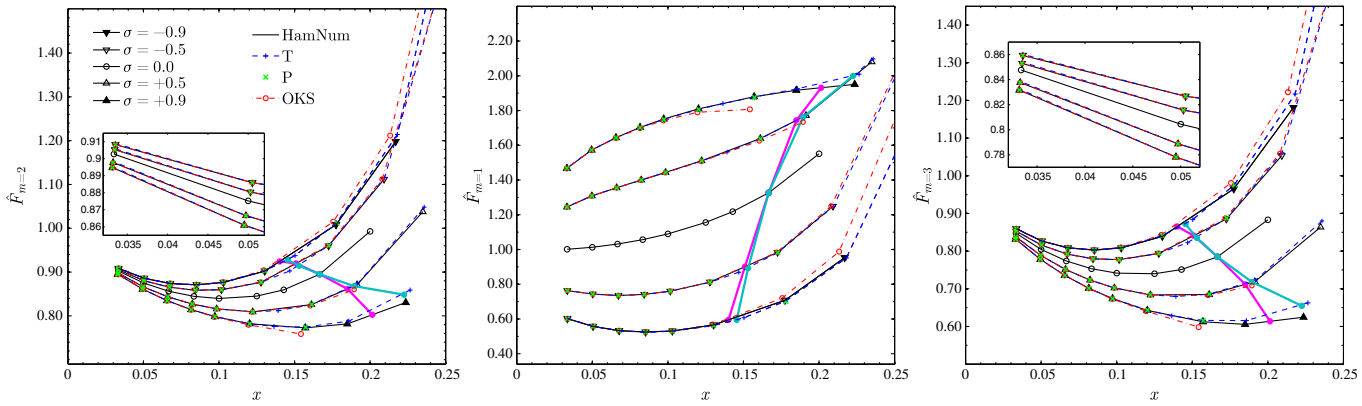

FIG. 6. Comparison of the multipolar $m = 2$ (left), $m = 1$ (center), and $m = 3$ (right) GW fluxes over x; see Fig. 4 for details.

of the fluxes from the Hamiltonian dynamics paves the way for applying a resummation/factorization procedure along the lines of Ref. [74] to post-Newtonian analytical test-particle waveforms that account for the spin.

Finally, we mention again that the $r = 30M$ T SSC results were obtained at higher resolutions than all other cases, which is why the relative differences in Tables V and VI seem larger and are thus shown in brackets.

VI. CONCLUSIONS

In this paper we have studied, for the first time, four different approaches for the dynamics of a spinning test body in circular equatorial orbits around a BH, namely i) MP with the T SSC, ii) MP with the P SSC, iii) MP with the OKS SSC, and iv) Hamiltonian dynamics based on the EOB Hamiltonian of Damour and Nagar [28]. For each case we have presented numerical procedures for finding initial data that upon evolution lead to circular orbits. Notably, this is the first time that CEOs have been studied within the OKS SSC, and the numerical procedure we used is novel, as is the one presented for the P SSC.

The analysis of energetics and the ISCO shift (coordinate-invariant quantities) indicated that all prescriptions are practically equivalent at small orbital frequencies $x \ll x_{\rm ISCO}$. This result is expected, but a numerical proof, and especially an analysis in the strong-field regime, were missing in the literature. For $\sigma \lesssim 0.2$, all different approaches remain very compatible up to the ISCO for negative spins (see Fig. 1). We also found agreement for large negative particle spins. For $\sigma > 0.2$, however, the dynamics exhibit drastic deviations. We found that, in this regime of large positive spins, the OKS SSC shows the most deviations from the Hamiltonian reference case; e.g., the spin-orbit contribution of the OKS SSC case and that of the Hamiltonian case differ by 10% for $|\sigma| = 0.9$ at $x \approx 0.17$.

We have also explored the influence of the different spinning test-body dynamics on the GW fluxes. This analysis provides an important tool to assess if the different dynamics are, in practice, equivalent. Consistently with the analysis of the energetics, we found that the GW fluxes of the different CEO dynamics are equivalent up to the 1% level even at moderately large particle frequencies $x \lesssim 0.15$ ($r \gtrsim 8M$). At larger distances the agreement is below our numerical uncertainty (0.2%), which gives confidence that indeed all prescriptions are compatible in the weak field. On the contrary, the disagreement at small x indicates that at the pole-dipole level the choice of SSC influences relevant features of the described physics.

The main practical application of this work lies in the context of modeling GW fluxes, as done, e.g., in the EOB model. The EOB model relies on an analytic radiation reaction force that accounts for the GW fluxes. This radiation reaction is found through elaborate resummation and factorization procedures [74,76], which currently do not incorporate the spin of the particle. The present study constitutes the first step towards including the spin by providing a numerical target solution that guides the resummation and is needed to assure success. While on the analytical side the literature contains all necessary post-Newtonian results on the multipolar waveforms [40,77–80], on the numerical side only the results for the T SSC dynamics exist [29]. Before the present study it was, however, unclear to what extent the T SSC dynamics would be compatible with the Hamiltonian dynamics that are related to the EOB approach. Therefore, the found equivalence of the various dynamics at large orbital distances is important since it means that a representation which is good for one case (say, the Hamiltonian dynamics) is also good for the other cases. However, close to the ISCO it will be essential in modeling the GW fluxes to actually use the fluxes obtained within the Hamiltonian dynamics.

A generalization of our results to the setup of a spinning test body orbiting around a rotating BH has been theoretically prepared in this work and will be explored in practice in a subsequent work. Furthermore, it would be interesting to check additional SSCs such as the Newton-Wigner SSC, and to include explicitly the canonical spinning particle Hamiltonian of Refs. [22,27] in the comparison. It is also

conceivable to focus on another class of orbits, e.g., radial infalls. As for CEOs, one would be able to compare the different SSCs for the same physical situation, and thus to get a further grasp on the implications and potential pathologies of the different approaches.

The data computed in this work, including multipolar fluxes and the key numbers of the dynamics as presented in Tables III–VI, are freely available in Ref. [81].

ACKNOWLEDGMENTS

We want to thank D. Bini, F. Costa, T. Damour, D. Hilditch, B. Brügmann, G. Schäfer, and M. Šrámek for useful discussions on the topic and helpful comments on the manuscript. Special thanks to O. Semerák for very enlightening discussions about MP and SSCs. We are particularly grateful to Scott Hughes for providing his data on circular orbits for a nonspinning particle. This work was supported in part by DFG grant SFB/Transregio 7 "Gravitational Wave Astronomy." E. H. thanks IHES for hospitality during the development of part of this work. G. L-G. is supported by UNCE-204020 and by GACR-14-10625S.

APPENDIX A: ISCOS FOR A NONSPINNING PARTICLE

The ISCO for a nonspinning particle is naturally found when writing the geodesic EOM in the radial direction in the form

$$\frac{1}{2}\left(\frac{dr}{d\lambda}\right)^2 + V_{\rm eff}(J_z, r) = \epsilon, \tag{A1}$$

where $V_{\rm eff}(J_z, r)$ is called the effective potential of radial motion and $\epsilon = \frac{1}{2}E^2$, with E being the conserved energy of the particle and J_z the conserved z component of its angular momentum. The form of Eq. (A1) is chosen so as to resemble the classical EOM of a harmonic oscillator with unit mass. For $V_{\rm eff}(J_z, r) = \epsilon$ one gets turning points of radial motion. For circular orbits the radial acceleration needs to vanish, which is the case at extrema of the radial potential, i.e., when

$$\frac{d}{dr}V_{\rm eff}(J_z, r) = 0. \tag{A2}$$

The circular orbit is stable/unstable when the extremum is a minimum/maximum. If we assume that the energy has the specific value corresponding to an ISCO, then for a given, sufficiently large value of J_z there are always two solutions to Eq. (A2): one radius at which the given J_z leads to a stable circular orbit and another one that leads to a unstable circular orbit. As J_z is decreased, these two solutions approach one another until they coincide. For smaller J_z circular orbits are ruled out because the particle has too little angular motion to prevent itself from falling into the BH. The solution of Eq. (A2) which is associated to the minimum possible value for J_z is typically understood as the ISCO. We note that this orbit corresponds to an inflection point of $V_{\rm eff}$, i.e., $\frac{d^2}{dr^2}V_{\rm eff} = 0$. Thus, the orbit is neither stable nor unstable in the sense explained above, and the term "innermost stable" circular orbit is actually a bit misleading. Therefore, we prefer to call that radius the "indifferently stable circular orbit."

To get an impression let us consider some values. For a background spin of $\hat{a} = -0.9$ one finds $r_{\rm ISCO} \approx 8.7$, for $\hat{a} = 0$ at $r_{\rm ISCO} = 6M$, and for $\hat{a} = 0.9$ at $r_{\rm ISCO} \approx 2.3M$. Thus, it depends on the background spin whether an orbit at, say, $r = 8M$ is a rather "strong-field" or "weak-field" orbit.

APPENDIX B: SOLUTION METHODS FOR CEOS AND ISCOS

We want to briefly explain the specific numerical solution methods that we employ for solving the equations that define CEOs and ISCOs, as derived in Sec. II.

In general we find it convenient to use the dimensionless particle spin $\sigma = S/(\mu M)$. If needed, one can rescale accordingly later. This means, however, that in the calculation we have to make all the other quantities dimensionless as well, e.g.,

$$\hat{r} = \frac{r}{M}, \qquad \hat{J}_z = \frac{J_z}{\mu M}, \qquad \hat{E} = \frac{E}{\mu}. \tag{B1}$$

The dimensionless quantities are equivalent to the dimensional quantities when one sets $\mu = M = 1$, as we do in practice. For more details see Sec. II C in Paper I. Note that for the P SSC one has to use the mass m instead of the mass μ, i.e., $\sigma = S/(\mathsf{m}M)$, since m is a constant of motion while μ is not (see Table I). Therefore, for the P SSC we set $\mathsf{m} = M = 1$ in our calculations.

To find CEOs for the MP with the T SSC, we solve the system (39) for a given radial distance r and spin S to get the energy E, and the z component of the total angular momentum, J_z. For simplicity, we solve the system using the routine `Solve` in MATHEMATICA. The latter gives the same result, up to machine precision, as the closed-form solution of Refs. [35,40]. To find an ISCO for a given spin S, we employ Eq. (39) along with the condition $\frac{d^2V_{\rm eff,T}}{dr^2} = 0$ and also use the `Solve` routine.

To find initial conditions for CEOs under the P and OKS SSCs, we have to solve the respective three potential systems described in Secs. II B 2 and II B 3. For the P SSC this is concretely the system (45); for the OKS SSC the three potentials are given in Eqs. (52), (54) and (56) and their derivatives with respect to r can be straightforwardly computed. In practice, to solve these systems we use a Newton-Raphson method as implemented with

`FindRoot` in MATHEMATICA. We used the Newton-Raphson method because the three potential systems are composed of equations which contain up to sixth-order polynomials in r and up to second-order polynomials in the rest of the unknowns. Alternatively, for the P SSC one can use `NSolve` to find CEOs; however, note that for the OKS SSC the `NSolve` misbehaves for large radii. To verify the ability of the novel three-potentials method to find CEOs (Secs. II B 2 and II B 3), several initial conditions have been evolved in time by the algorithm implemented already in Ref. [21] and Paper I. The orbits have been found to be circular up to numerical accuracy.

Concerning the location of the ISCOs, we have used three different approaches to test the ability of the three-potentials method to find them, and these approaches give results which agree up to numerical accuracy.

(a) First, we simply employed `FindRoot` in MATHEMATICA for a given σ to solve the system (45) along with Eq. (46) for the P SSC, and the equivalent system for the OKS SSC. Since the numerical method for solving does not provide a unique solution, we have chosen those solutions which appeared to be the nearest to the analogue solution found for the T SSC for the given σ (Table II shows these solutions).

TABLE III. Comparison of the dynamical quantities Ω and v^t for circular, equatorial orbits of a spinning particle around a Schwarzschild BH for four different prescriptions of the dynamics: i) Hamiltonian dynamics (Ham), ii) MP with the T SSC, iii) MP with the P SSC, iv) MP with the OKS SSC. The different cases are indicated as subscripts in the respective quantities. The values are normalized by setting $\mu = M = 1$. As the orbital distance increases all dynamics become equivalent. At $r = 30M$ we see no differences in the shown five digits. At small radii, the Hamiltonian dynamics and the MP with the T SSC are still very much the same, while the MP with the OKS SSC becomes more significantly different. Note that v^ϕ can be computed from the given quantities.

$\hat{a} = 0.00$

$\hat{r}$	σ	$M\Omega_{\rm Ham}$	$M\Omega_{\rm T}$	$M\Omega_{\rm P}$	$M\Omega_{\rm OKS}$	$v^t_{\rm Ham}$	$v^t_{\rm T}$	$v^t_{\rm T}$	$v^t_{\rm OKS}$
4.00	−0.90	0.14676	0.15052	/	0.14013	2.53679	2.69700	/	2.31987
	−0.50	/	0.13805	/	0.13451	/	2.26404	/	2.17945
	0.50	0.11382	0.11452	0.11433	/	1.84835	1.85641	1.85419	/
	0.90	0.10573	0.10780	0.10692	/	1.76463	1.78435	1.77588	/
5.00	−0.90	0.10104	0.10184	0.10238	0.09850	1.70303	1.71313	1.72019	1.67265
	−0.50	0.09570	0.09592	0.09600	0.09484	1.64173	1.64407	1.64483	1.63266
	0.50	0.08372	0.08390	0.08386	0.08246	1.53432	1.53570	1.53538	1.52494
	0.90	0.07952	0.08009	0.07988	/	1.50428	1.50821	1.50672	/
6.00	−0.90	0.07475	0.07498	0.07512	0.07360	1.46568	1.46766	1.46878	1.45613
	−0.50	0.07166	0.07172	0.07174	0.07128	1.44066	1.44117	1.44132	1.43777
	0.50	0.06471	0.06477	0.06476	0.06425	1.39223	1.39261	1.39252	1.38937
	0.90	0.06224	0.06244	0.06237	0.06055	1.37722	1.37840	1.37797	1.36760
8.00	−0.90	0.04698	0.04702	0.04704	0.04666	1.28172	1.28193	1.28205	1.27969
	−0.50	0.04571	0.04572	0.04572	0.04560	1.27381	1.27387	1.27389	1.27319
	0.50	0.04277	0.04279	0.04278	0.04266	1.25699	1.25705	1.25704	1.25639
	0.90	0.04170	0.04174	0.04172	0.04133	1.25126	1.25145	1.25139	1.24932
10.00	−0.90	0.03303	0.03304	0.03305	0.03291	1.20309	1.20314	1.20316	1.20241
	−0.50	0.03239	0.03239	0.03239	0.03235	1.19945	1.19946	1.19947	1.19924
	0.50	0.03089	0.03089	0.03089	0.03085	1.19134	1.19135	1.19135	1.19114
	0.90	0.03033	0.03034	0.03034	0.03020	1.18845	1.18849	1.18848	1.18779
12.00	−0.90	0.02487	0.02487	0.02487	0.02481	1.15911	1.15913	1.15913	1.15882
	−0.50	0.02450	0.02450	0.02450	0.02448	1.15709	1.15709	1.15709	1.15700
	0.50	0.02363	0.02363	0.02363	0.02361	1.15246	1.15246	1.15246	1.15237
	0.90	0.02330	0.02330	0.02330	0.02325	1.15076	1.15077	1.15077	1.15047
15.00	−0.90	0.01762	0.01762	0.01762	0.01760	1.12029	1.12029	1.12029	1.12018
	−0.50	0.01744	0.01744	0.01744	0.01743	1.11926	1.11926	1.11927	1.11923
	0.50	0.01699	0.01699	0.01699	0.01699	1.11686	1.11686	1.11686	1.11683
	0.90	0.01682	0.01682	0.01682	0.01680	1.11595	1.11596	1.11596	1.11585
20.00	−0.90	0.01135	0.01135	0.01135	0.01135	1.08564	1.08564	1.08564	1.08561
	−0.50	0.01127	0.01128	0.01128	0.01127	1.08520	1.08520	1.08520	1.08519
	0.50	0.01109	0.01109	0.01109	0.01109	1.08413	1.08413	1.08413	1.08412
	0.90	0.01101	0.01101	0.01101	0.01101	1.08371	1.08371	1.08371	1.08368
30.00	−0.90	0.00614	0.00614	0.00614	0.00614	1.05442	1.05442	1.05442	1.05441
	−0.50	0.00611	0.00611	0.00611	0.00611	1.05427	1.05427	1.05427	1.05427
	0.50	0.00606	0.00606	0.00606	0.00606	1.05392	1.05392	1.05392	1.05391
	0.90	0.00604	0.00604	0.00604	0.00604	1.05378	1.05378	1.05378	1.05377

(b) For the second approach, we used the $a = \sigma = 0$ analytically known solution as an initial guess for the `FindRoot` when $|\sigma|$ had a very small nonzero value to calculate the new corresponding ISCO solution of the three-potential system. This new solution was then fed to `FindRoot` as an initial guess to find a solution for a little bit larger value of $|\sigma|$, and so on until $|\sigma| \approx 1$ had been reached (see, e.g., Fig. 3).

(c) Finally, we used the CEOs' $E(J_z)$ plots for a given σ to see where a cusp appears. A cusp appears when the ISCO is reached and since the $E(J_z)$ plots depend on radius one can find the ISCO radius.

Note that in general the potential systems provide more than one solution for CEOs. We have chosen to work with the solutions for which $1 \gtrsim E > 0$, $J_z > 0$, $0 < V_t \sim -E$, and $0 < V_\phi \sim J_z$. This applies to all three SSCs tested, so that V_μ here refers to the reference vector in general, and it has to be adopted appropriately according to the SSC.

APPENDIX C: ANALYSIS OF DYNAMICAL DATA

In order to assure ourselves that our CEO initial data routines (cf. Secs. II B and III D) are indeed correct, we have integrated the respective EOM numerically as explained in Ref. [21].

Having produced CEOs for all the different dynamical approaches, an inspection of the data reveals that most of the variables (1) are vanishing. In particular, for CEOs all

TABLE IV. Comparison of the dynamical quantities p^t and p^ϕ for circular, equatorial orbits of a spinning particle around a Schwarzschild BH. See caption of Table III for details.

$\hat{a} = 0.00$

$\hat{r}$	σ	$p^t_{\rm Ham}$	$p^t_{\rm T}$	$p^t_{\rm P}$	$p^t_{\rm OKS}$	$p^\phi_{\rm Ham}$	$p^\phi_{\rm T}$	$p^\phi_{\rm P}$	$p^\phi_{\rm OKS}$
4.00	−0.90	2.53679	2.47059	/	2.31987	0.37230	0.35811	/	0.32509
	−0.50	/	2.22421	/	2.17945	/	0.30348	/	0.29315
	0.50	1.84835	1.84108	1.83930	/	0.21039	0.20838	0.20792	/
	0.90	1.76463	1.74715	1.73973	/	0.18658	0.18136	0.17931	/
5.00	−0.90	1.70303	1.68888	1.69109	1.67265	0.17207	0.16869	0.16929	0.16476
	−0.50	1.64173	1.63802	1.63834	1.63266	0.15712	0.15619	0.15627	0.15483
	0.50	1.53432	1.53192	1.53170	1.52494	0.12845	0.12776	0.12770	0.12574
	0.90	1.50428	1.49786	1.49676	/	0.11962	0.11767	0.11736	/
6.00	−0.90	1.46568	1.46060	1.46097	1.45613	0.10956	0.10830	0.10840	0.10718
	−0.50	1.44066	1.43926	1.43932	1.43777	0.10323	0.10287	0.10289	0.10249
	0.50	1.39223	1.39120	1.39115	1.38937	0.09009	0.08980	0.08978	0.08927
	0.90	1.37722	1.37434	1.37406	1.36760	0.08572	0.08485	0.08478	0.08281
8.00	−0.90	1.28172	1.28053	1.28057	1.27969	0.06022	0.05992	0.05993	0.05971
	−0.50	1.27381	1.27346	1.27347	1.27319	0.05822	0.05813	0.05813	0.05806
	0.50	1.25699	1.25671	1.25670	1.25639	0.05377	0.05369	0.05369	0.05360
	0.90	1.25126	1.25042	1.25039	1.24932	0.05218	0.05194	0.05193	0.05163
10.00	−0.90	1.20309	1.20268	1.20268	1.20241	0.03974	0.03964	0.03964	0.03958
	−0.50	1.19945	1.19933	1.19933	1.19924	0.03885	0.03882	0.03882	0.03880
	0.50	1.19134	1.19123	1.19123	1.19114	0.03680	0.03677	0.03677	0.03675
	0.90	1.18845	1.18812	1.18811	1.18779	0.03604	0.03596	0.03596	0.03587
12.00	−0.90	1.15911	1.15893	1.15893	1.15882	0.02882	0.02878	0.02878	0.02875
	−0.50	1.15709	1.15704	1.15704	1.15700	0.02835	0.02833	0.02833	0.02833
	0.50	1.15246	1.15241	1.15241	1.15237	0.02723	0.02722	0.02722	0.02721
	0.90	1.15076	1.15061	1.15060	1.15047	0.02681	0.02678	0.02678	0.02674
15.00	−0.90	1.12029	1.12022	1.12022	1.12018	0.01974	0.01973	0.01973	0.01972
	−0.50	1.11926	1.11924	1.11924	1.11923	0.01952	0.01951	0.01951	0.01951
	0.50	1.11686	1.11684	1.11684	1.11683	0.01898	0.01898	0.01898	0.01897
	0.90	1.11595	1.11589	1.11589	1.11585	0.01877	0.01876	0.01876	0.01875
20.00	−0.90	1.08564	1.08562	1.08562	1.08561	0.01232	0.01232	0.01232	0.01232
	−0.50	1.08520	1.08519	1.08519	1.08519	0.01224	0.01223	0.01223	0.01223
	0.50	1.08413	1.08412	1.08412	1.08412	0.01202	0.01202	0.01202	0.01202
	0.90	1.08371	1.08370	1.08370	1.08368	0.01194	0.01193	0.01193	0.01193
30.00	−0.90	1.05442	1.05441	1.05441	1.05441	0.00647	0.00647	0.00647	0.00647
	−0.50	1.05427	1.05427	1.05427	1.05427	0.00645	0.00645	0.00645	0.00645
	0.50	1.05392	1.05391	1.05391	1.05391	0.00638	0.00638	0.00638	0.00638
	0.90	1.05378	1.05377	1.05377	1.05377	0.00636	0.00636	0.00636	0.00636

TABLE V. Comparison of energy fluxes in the $m = 2$ and $m = 1$ modes produced by a spinning particle for four different circular dynamics: i) Hamiltonian dynamics (Ham), ii) MP with the T SSC, iii) MP with the P SSC, iv) MP with the OKS SSC. We use the Hamiltonian case as the reference when computing the respective differences shown in the $\Delta[\%]$ columns. In case the relative differences fall below the level of 0.001% we do just write $< 0.001\%$ to avoid citing more digits. If a certain combination was not simulated we write a backslash /. The T SSC results for $r = 30M$ were obtained at higher resolutions than all the other cases, see discussion in Sec. V A, which is why the relative differences are not consistent and thus shown in brackets. The table compares the fluxes in the $m = 1$ and $m = 2$ modes at several Boyer-Lindquist radii r and for the four particle spins $\sigma = \pm 0.9 \pm 0.5$. The values for the energy fluxes have to be understood as normalized by the leading order Newtonian flux, cf. Eq. (104). The main observation is that the relative differences between the respective fluxes vanish as the orbital distance grows. At $r = 20M$ the energy fluxes from all dynamics agree in all measured cases up to $\lesssim 0.1\%$ or better.

$\hat{a} = 0.00$

$\hat{r}$	σ	$\hat{F}^{\mathrm{Ham}}_{m=2}$	$\hat{F}^{\mathrm{T}}_{m=2}$	$\Delta[\%]$	$\hat{F}^{\mathrm{P}}_{m=2}$	$\Delta[\%]$	$\hat{F}^{\mathrm{OKS}}_{m=2}$	$\Delta[\%]$	$\hat{F}^{\mathrm{Ham}}_{m=1}$	$\hat{F}^{\mathrm{T}}_{m=1}$	$\Delta[\%]$	$\hat{F}^{\mathrm{P}}_{m=1}$	$\Delta[\%]$	$\hat{F}^{\mathrm{OKS}}_{m=1}$	$\Delta[\%]$
4.00	−0.90	/	2.218	/	/	/	2.054	/	/	2.153	/	/	/	2.151	/
	−0.50	/	1.802	/	/	/	1.741	/	/	2.298	/	/	/	2.242	/
	0.50	1.038	1.048	1.017	/	/	/	/	2.080	2.097	0.808	/	/	/	/
	0.90	0.830	0.859	3.430	/	/	/	/	1.951	2.009	3.004	/	/	/	/
5.00	−0.90	1.198	1.214	1.330	/	/	1.212	1.132	0.953	0.951	0.170	/	/	0.988	3.646
	−0.50	1.112	1.115	0.324	/	/	1.112	0.013	1.249	1.248	0.057	/	/	1.249	0.047
	0.50	0.871	0.873	0.232	/	/	0.860	1.242	1.772	1.772	0.053	/	/	1.733	2.147
	0.90	0.782	0.788	0.804	/	/	/	/	1.917	1.925	0.441	/	/	/	/
6.00	−0.90	1.008	1.013	0.457	1.012	0.420	1.015	0.705	0.708	0.703	0.699	0.701	1.011	0.720	1.721
	−0.50	0.960	0.961	0.105	0.961	0.105	0.961	0.084	0.983	0.982	0.176	0.981	0.190	0.984	0.028
	0.50	0.826	0.826	0.067	0.826	0.057	0.823	0.313	1.639	1.638	0.071	1.637	0.093	1.625	0.836
	0.90	0.773	0.774	0.232	0.774	0.164	0.759	1.810	1.879	1.878	0.074	1.875	0.230	1.807	3.846
8.00	−0.90	0.902	0.903	0.071	0.903	0.063	0.904	0.210	0.566	0.563	0.519	0.562	0.577	0.568	0.444
	−0.50	0.877	0.877	0.014	0.877	0.014	0.877	0.034	0.812	0.811	0.128	0.811	0.132	0.812	0.019
	0.50	0.809	0.809	0.005	0.809	0.004	0.809	0.049	1.511	1.510	0.073	1.510	0.076	1.507	0.264
	0.90	0.782	0.782	0.017	0.782	0.008	0.780	0.285	1.809	1.806	0.175	1.806	0.206	1.790	1.097
10.00	−0.90	0.876	0.876	0.010	0.876	0.008	0.877	0.076	0.531	0.529	0.311	0.529	0.327	0.532	0.136
	−0.50	0.860	0.860	< 0.001	0.860	< 0.001	0.860	0.013	0.760	0.759	0.078	0.759	0.078	0.760	0.022
	0.50	0.816	0.816	0.002	0.816	0.002	0.816	0.014	1.444	1.443	0.048	1.443	0.048	1.442	0.121
	0.90	0.798	0.798	0.008	0.798	0.010	0.798	0.083	1.751	1.749	0.128	1.749	0.137	1.743	0.485
12.00	−0.90	0.871	0.871	0.002	0.871	0.003	0.871	0.032	0.525	0.524	0.194	0.524	0.203	0.525	0.041
	−0.50	0.859	0.859	0.002	0.859	0.002	0.859	0.005	0.741	0.741	0.050	0.741	0.048	0.741	0.016
	0.50	0.827	0.827	0.002	0.827	0.002	0.827	0.005	1.400	1.399	0.034	1.399	0.034	1.399	0.067
	0.90	0.814	0.814	0.010	0.814	0.010	0.814	0.033	1.703	1.701	0.089	1.701	0.089	1.698	0.258
15.00	−0.90	0.874	0.874	0.005	0.874	0.005	0.874	0.010	0.533	0.532	0.114	0.532	0.122	0.533	0.004
	−0.50	0.865	0.865	0.001	0.865	0.002	0.865	0.002	0.735	0.735	0.020	0.735	0.022	0.735	0.009
	0.50	0.844	0.844	0.002	0.844	0.002	0.844	0.002	1.355	1.355	0.013	1.355	0.019	1.355	0.037
	0.90	0.835	0.835	0.007	0.835	0.006	0.835	0.011	1.644	1.643	0.048	1.643	0.052	1.642	0.129
20.00	−0.90	0.886	0.886	0.002	0.886	0.002	0.886	0.002	0.557	0.557	0.010	0.557	0.021	0.557	0.020
	−0.50	0.880	0.880	0.001	0.880	0.001	0.880	< 0.001	0.743	0.743	0.017	0.743	0.020	0.743	0.012
	0.50	0.867	0.867	0.002	0.867	0.002	0.867	0.002	1.309	1.309	0.005	1.309	0.008	1.308	0.017
	0.90	0.861	0.861	0.003	0.861	0.004	0.861	0.003	1.572	1.572	0.013	1.572	0.001	1.572	0.043
30.00	−0.90	0.908	0.909	(0.065)	0.908	< 0.001	0.908	< 0.001	0.602	0.603	(0.230)	0.601	0.117	0.601	0.029
	−0.50	0.905	0.906	(0.071)	0.905	< 0.001	0.905	0.002	0.763	0.764	(0.185)	0.763	0.011	0.763	0.003
	0.50	0.898	0.898	(0.065)	0.898	0.003	0.898	0.002	1.245	1.246	(0.129)	1.244	0.015	1.244	0.014
	0.90	0.895	0.895	(0.065)	0.895	< 0.001	0.895	< 0.001	1.467	1.469	(0.163)	1.468	0.049	1.466	0.038

time derivatives are zero, with $\frac{d}{dt}\phi \equiv \Omega$ being the only exception. From the list (1) only the four quantities

$$\{v^t, v^\phi, p_t, p_\phi\} \tag{C1}$$

are nontrivial. The other components of v^μ and p_μ are zero, and the spin tensor can be computed from the spin parameter σ using Eq. (35). Note that one can compute Ω from v^t and v^ϕ.

To summarize our dynamics, Table III lists our results for Ω and v^t, for the four different dynamical approaches and for all configurations of (r, σ) tested; Table IV analogously lists the values for p^t, p^ϕ. Notably, these tables will enable future studies to check our flux computations of Sec. V

TABLE VI. Complement of Table V for the $m = 3$ mode. See caption of Table V for details.

$\hat{a} = 0.00$								
$\hat{r}$	σ	$\hat{F}^{\mathrm{Ham}}_{m=3}$	$\hat{F}^{\mathrm{T}}_{m=3}$	$\Delta[\%]$	$\hat{F}^{\mathrm{P}}_{m=3}$	$\Delta[\%]$	$\hat{F}^{\mathrm{OKS}}_{m=3}$	$\Delta[\%]$
4.00	−0.90	/	2.425	/	/	/	2.249	/
	−0.50	/	1.840	/	/	/	1.776	/
	0.50	0.864	0.880	1.892	/	/	/	/
	0.90	0.625	0.663	6.077	/	/	/	/
5.00	−0.90	1.181	1.217	3.032	/	/	1.222	3.462
	−0.50	1.053	1.061	0.743	/	/	1.059	0.525
	0.50	0.719	0.722	0.511	/	/	0.708	1.460
	0.90	0.606	0.616	1.646	/	/	/	/
6.00	−0.90	0.965	0.976	1.123	0.975	1.054	0.981	1.650
	−0.50	0.885	0.887	0.273	0.887	0.272	0.888	0.303
	0.50	0.685	0.686	0.183	0.686	0.171	0.682	0.326
	0.90	0.613	0.616	0.582	0.616	0.491	0.598	2.332
8.00	−0.90	0.839	0.841	0.228	0.841	0.215	0.843	0.459
	−0.50	0.794	0.794	0.055	0.794	0.054	0.794	0.095
	0.50	0.684	0.684	0.035	0.684	0.034	0.684	0.035
	0.90	0.643	0.643	0.107	0.643	0.096	0.641	0.314
10.00	−0.90	0.808	0.809	0.062	0.809	0.058	0.810	0.168
	−0.50	0.777	0.777	0.015	0.777	0.014	0.778	0.036
	0.50	0.702	0.702	0.008	0.702	0.008	0.702	0.005
	0.90	0.674	0.674	0.023	0.674	0.021	0.673	0.077
12.00	−0.90	0.803	0.803	0.019	0.803	0.018	0.803	0.073
	−0.50	0.779	0.780	0.004	0.780	0.004	0.780	0.016
	0.50	0.723	0.723	0.001	0.723	0.001	0.723	0.001
	0.90	0.701	0.701	0.003	0.701	0.003	0.701	0.026
15.00	−0.90	0.809	0.809	0.002	0.809	0.002	0.809	0.025
	−0.50	0.792	0.792	< 0.001	0.792	< 0.001	0.792	0.005
	0.50	0.751	0.751	< 0.001	0.751	< 0.001	0.751	< 0.001
	0.90	0.736	0.736	0.003	0.736	0.003	0.736	0.009
20.00	−0.90	0.827	0.827	0.003	0.827	0.003	0.827	0.006
	−0.50	0.816	0.816	< 0.001	0.816	< 0.001	0.816	0.002
	0.50	0.789	0.789	< 0.001	0.789	0.001	0.789	0.002
	0.90	0.778	0.778	< 0.001	0.778	0.002	0.778	0.001
30.00	−0.90	0.859	0.860	(0.098)	0.859	0.007	0.859	< 0.001
	−0.50	0.853	0.854	(0.114)	0.853	0.006	0.853	0.006
	0.50	0.838	0.839	(0.103)	0.838	0.002	0.838	0.004
	0.90	0.832	0.833	(0.101)	0.832	0.002	0.832	< 0.001

without the need to recompute the dynamics. Let us look at Tables III and IV to analyze our results. The main observation is that the different dynamical approaches rapidly converge to the same solution for $\{\Omega, v^t, p_t, p_\phi\}$ as the radius increases. For example, looking at Ω at $r = 30M$, the four different approaches are equivalent at least in the first three significant digits. The same holds for v^t, p_t, and p_ϕ. The equivalence is still surprisingly good at medium distances; at $r = 10M$, for instance, v^t varys at most by $\sim 0.05\%$ between the four prescriptions. At even smaller distances the quantities slowly start to diverge from one another. In general one observes that the T and P SSCs yield values which are closest together, with the Hamiltonian approach still being quite compatible; the OKS SSC values deviate the most. Looking at Eq. (17), the similarity of the T and P SSCs can be expected at large radii, where the curvature is small, but it is remarkable how much it holds at rather small radii. After all, we conclude that the four different approaches converge to a unique result for CEOs at large orbital distances. Thus it is clear that the GW fluxes also have to be the same for CEOs in the weak field.

[1] M. Mathisson, Neue mechanik materieller systemes, Acta Phys. Pol. **6**, 163 (1937); Republication of: New mechanics of material systems, Gen. Relativ. Gravit. **42**, 1011 (2010).

[2] A. Papapetrou, Spinning test particles in general relativity. 1, Proc. R. Soc. A **209**, 248 (1951).

[3] M. Mathisson, New mechanics of material systems, Gen. Relativ. Gravit. **42**, 1011 (2010).

[4] W Tulczyjew, Motion of multipole particles in general relativity theory, Acta. Phys. Pol. **18**, 393 (1959).

[5] J. Steinhoff, Canonical formulation of spin in general relativity, Ann. Phys. (Amsterdam) **523**, 296 (2011).

[6] T. Hinderer *et al.*, Periastron advance in spinning black hole binaries: Comparing effective-one-body and numerical relativity, Phys. Rev. D **88**, 084005 (2013).

[7] D. Bini, P. Fortini, A. Geralico, and A. Ortolan, Quadrupole effects on the motion of extended bodies in Kerr spacetime, Classical Quantum Gravity **25**, 125007 (2008).

[8] D. Bini and A. Geralico, Deviation of quadrupolar bodies from geodesic motion in a Kerr spacetime, Phys. Rev. D **89**, 044013 (2014).

[9] D. Bini and A. Geralico, Dynamics of quadrupolar bodies in a Schwarzschild spacetime, Phys. Rev. D **87**, 024028 (2013).

[10] D. Bini and A. Geralico, Effect of an arbitrary spin orientation on the quadrupolar structure of an extended body in a Schwarzschild spacetime, Phys. Rev. D **91**, 104036 (2015).

[11] W. G. Dixon, A covariant multipole formalism for extended test bodies in general relativity, Nuovo Cimento **34**, 317 (1964).

[12] W. G. Dixon, Dynamics of extended bodies in general relativity. I. Momentum and angular momentum, Proc. R. Soc. A **314**, 499 (1970).

[13] W. G. Dixon, Dynamics of extended bodies in general relativity. II. Moments of the charge-current vector, Proc. R. Soc. A **319**, 509 (1970).

[14] W. G. Dixon, Dynamics of extended bodies in general relativity. III. Equations of motion, Phil. Trans. R. Soc. A **277**, 59 (1974).

[15] R. M. Wald, Gravitational spin interaction, Phys. Rev. D **6**, 406 (1972).

[16] K Kyrian and O Semerák, Spinning test particles in a Kerr field, Mon. Not. R. Astron. Soc. **382**, 1922 (2007).

[17] E. Corinaldesi and A. Papapetrou, Spinning test particles in general relativity. 2, Proc. R. Soc. A **209**, 259 (1951).

[18] T. D. Newton and E. P. Wigner, Localized states for elementary systems, Rev. Mod. Phys. **21**, 400 (1949).

[19] F. A. E. Pirani, On the physical significance of the Riemann tensor, Acta Phys. Pol. **15**, 389 (1956).

[20] A. Ohashi, Multipole particle in relativity, Phys. Rev. D **68**, 044009 (2003).

[21] G. Lukes-Gerakopoulos, J. Seyrich, and D. Kunst, Investigating spinning test particles: Spin supplementary conditions and the Hamiltonian formalism, Phys. Rev. D **90**, 104019 (2014).

[22] E. Barausse, E. Racine, and A. Buonanno, Hamiltonian of a spinning test-particle in curved spacetime, Phys. Rev. D **80**, 104025 (2009).

[23] E. Barausse and A. Buonanno, An improved effective-one-body Hamiltonian for spinning black-hole binaries, Phys. Rev. D **81**, 084024 (2010).

[24] W. G. Ramírez, A. A. Deriglazov, and A. M. Pupasov-Maksimov, Frenkel electron and a spinning body in a curved background, J. High Energy Phys. 03 (2014) 109.

[25] D. Kunst, T. Ledvinka, G. Lukes-Gerakopoulos, and J. Seyrich, Comparing Hamiltonians of a spinning test particle for different tetrad fields, Phys. Rev. D **93**, 044004 (2016).

[26] D. Bini, T. Damour, and A. Geralico, Spin-dependent two-body interactions from gravitational self-force computations, Phys. Rev. D **92**, 124058 (2015).

[27] J. Vines, D. Kunst, Jan Steinhoff, and T. Hinderer, Canonical Hamiltonian for an extended test body in curved spacetime: To quadratic order in spin, Phys. Rev. D **93**, 103008 (2016).

[28] T. Damour and A. Nagar, New effective-one-body description of coalescing nonprecessing spinning black-hole binaries, Phys. Rev. D **90**, 044018 (2014).

[29] E. Harms, G. Lukes-Gerakopoulos, S. Bernuzzi, and A. Nagar, Asymptotic gravitational wave fluxes from a spinning particle in circular equatorial orbits around a rotating black hole, Phys. Rev. D **93**, 044015 (2016).

[30] D. Bini, G. Faye, and A. Geralico, Dynamics of extended bodies in a Kerr spacetime with spin-induced quadrupole tensor, Phys. Rev. D **92**, 104003 (2015).

[31] O. Semerák and M. Šrámek, Spinning particles in vacuum spacetimes of different curvature types, Phys. Rev. D **92**, 064032 (2015).

[32] S. E. Gralla, A. I. Harte, and R. M. Wald, Bobbing and kicks in electromagnetism and gravity, Phys. Rev. D **81**, 104012 (2010).

[33] O. Semerak, Spinning test particles in a Kerr field. 1, Mon. Not. R. Astron. Soc. **308**, 863 (1999).

[34] W.-B. Han, Gravitational waves from extreme-mass-ratio inspirals in equatorially eccentric orbits, Int. J. Mod. Phys. D **23**, 1450064 (2014).

[35] E. Hackmann, C. Laemmerzahl, Y. N. Obukhov, D. Puetzfeld, and I. Schaffer, Motion of spinning test bodies in Kerr spacetime, Phys. Rev. D **90**, 064035 (2014).

[36] M. Saijo, K.-i. Maeda, M. Shibata, and Y. Mino, Gravitational waves from a spinning particle plunging into a Kerr black hole, Phys. Rev. D **58**, 064005 (1998).

[37] M. D. Hartl, A Survey of spinning test particle orbits in Kerr space-time, Phys. Rev. D **67**, 104023 (2003).

[38] W.-B. Han, Gravitational radiations from a spinning compact object around a supermassive Kerr black hole in circular orbit, Phys. Rev. D **82**, 084013 (2010).

[39] U. Ruangsri, S. J. Vigeland, and S. A. Hughes, Gyroscopes orbiting black holes: A frequency-domain approach to precession and spin-curvature coupling for spinning bodies on generic Kerr orbits, Phys. Rev. D **94**, 044008 (2016).

[40] T. Tanaka, Y. Mino, M. Sasaki, and M. Shibata, Gravitational waves from a spinning particle in circular orbits around a rotating black hole, Phys. Rev. D **54**, 3762 (1996).

[41] L. F. Costa, C. Herdeiro, J. Natário, and M. Zilhão, Mathisson's helical motions for a spinning particle: Are they unphysical?, Phys. Rev. D **85**, 024001 (2012).

[42] Y. Pan, A. Buonanno, A. Taracchini, L. E. Kidder, A. H. Mroué, H. P. Pfeiffer, M. A. Scheel, and B. Szilágyi, Inspiral-merger-ringdown waveforms of spinning, precessing black-hole binaries in the effective-one-body formalism, Phys. Rev. D **89**, 084006 (2014).

[43] A. Taracchini *et al.*, Effective-one-body model for black-hole binaries with generic mass ratios and spins, Phys. Rev. D **89**, 061502 (2014).
[44] S. Babak, A. Taracchini, and A. Buonanno, Validating the effective-one-body model of spinning, precessing binary black holes against numerical relativity, arXiv:1607.05661.
[45] S. Balmelli and T. Damour, New effective-one-body Hamiltonian with next-to-leading order spin-spin coupling, Phys. Rev. D **92**, 124022 (2015).
[46] J. Steinhoff and D. Puetzfeld, Influence of internal structure on the motion of test bodies in extreme mass ratio situations, Phys. Rev. D **86**, 044033 (2012).
[47] S. Bernuzzi, T. Dietrich, W. Tichy, and B. Bruegmann, Mergers of binary neutron stars with realistic spin, Phys. Rev. D **89**, 104021 (2014).
[48] L. Filipe O. Costa and J. Natário, *Equations of Motion in Relativistic Gravity* (Springer, New York, 2015), p. 215.
[49] Y. Mino, M. Shibata, and T. Tanaka, Gravitational waves induced by a spinning particle falling into a rotating black hole, Phys. Rev. D **53**, 622 (1996).
[50] K. Tominaga, M. Saijo, and K.-i. Maeda, Gravitational waves from a spinning particle scattered by a relativistic star: Axial mode case, Phys. Rev. D **63**, 124012 (2001).
[51] K. Tominaga, M. Saijo, and K.-i. Maeda, Gravitational waves from a test particle scattered by a neutron star: Axial mode case, Phys. Rev. D **60**, 024004 (1999).
[52] L. M. Burko and G. Khanna, Self-force gravitational waveforms for extreme and intermediate mass ratio inspirals. III: Spin-orbit coupling revisited, Phys. Rev. D **91**, 104017 (2015).
[53] S. Bernuzzi and A. Nagar, Binary black hole merger in the extreme-mass-ratio limit: A multipolar analysis, Phys. Rev. D **81**, 084056 (2010).
[54] S. Bernuzzi, A. Nagar, and A. Zenginoğlu, Binary black hole coalescence in the large-mass-ratio limit: The hyperboloidal layer method and waveforms at null infinity, Phys. Rev. D **84**, 084026 (2011).
[55] E. Harms, S. Bernuzzi, and B. Brügmann, Numerical solution of the $2+1$ Teukolsky equation on a hyperboloidal and horizon penetrating foliation of Kerr and application to late-time decays, Classical Quantum Gravity **30**, 115013 (2013).
[56] E. Harms, S. Bernuzzi, A. Nagar, and A. Zenginoğlu, A new gravitational wave generation algorithm for particle perturbations of the Kerr spacetime, Classical Quantum Gravity **31**, 245004 (2014).
[57] S. A. Teukolsky, Rotating black holes—separable wave equations for gravitational and electromagnetic perturbations, Phys. Rev. Lett. **29**, 1114 (1972).
[58] S. A. Teukolsky, Perturbations of a rotating black hole. 1. Fundamental equations for gravitational electromagnetic and neutrino field perturbations, Astrophys. J. **185**, 635 (1973).
[59] G. Calabrese, C. Gundlach, and D. Hilditch, Asymptotically null slices in numerical relativity: Mathematical analysis and spherical wave equation tests, Classical Quantum Gravity **23**, 4829 (2006).
[60] A. Zenginoğlu, Hyperboloidal foliations and scri-fixing, Classical Quantum Gravity **25**, 145002 (2008).
[61] A. Zenginoğlu and M. Tiglio, Spacelike matching to null infinity, Phys. Rev. D **80**, 024044 (2009).
[62] A. Zenginoğlu, Hyperboloidal layers for hyperbolic equations on unbounded domains, J. Comput. Phys. **230**, 2286 (2011).
[63] A. Vañó-Viñuales, S. Husa, and D. Hilditch, Spherical symmetry as a test case for unconstrained hyperboloidal evolution, Classical Quantum Gravity **32**, 175010 (2015).
[64] S. Bernuzzi, A. Nagar, and A. Zenginoğlu, Horizon-absorption effects in coalescing black-hole binaries: An effective-one-body study of the non-spinning case, Phys. Rev. D **86**, 104038 (2012).
[65] S. Bernuzzi, A. Nagar, and A. Zenginoğlu, Binary black hole coalescence in the extreme-mass-ratio limit: testing and improving the effective-one-body multipolar waveform, Phys. Rev. D **83**. 064010 (2011).
[66] E. Barausse, A. Buonanno, S. A. Hughes, G. Khanna, S. O'Sullivan, and Y. Pan, Modeling multipolar gravitational-wave emission from small mass-ratio mergers, Phys. Rev. D **85**, 024046 (2012).
[67] P. A. Sundararajan, G. Khanna, and S. A. Hughes, Binary black hole merger gravitational waves and recoil in the large mass ratio limit, Phys. Rev. D **81**, 104009 (2010).
[68] P. A. Sundararajan, G. Khanna, and S. A. Hughes, Towards adiabatic waveforms for inspiral into Kerr black holes: I. A new model of the source for the time domain perturbation equation, Phys. Rev. D **76**, 104005 (2007).
[69] S. A. Hughes, The evolution of circular, nonequatorial orbits of Kerr black holes due to gravitational wave emission, Phys. Rev. D **61**, 084004 (2000).
[70] A. Taracchini, A. Buonanno, G. Khanna, and S. A. Hughes, Small mass plunging into a Kerr black hole: Anatomy of the inspiral-merger-ringdown waveforms, Phys. Rev. D **90**, 084025 (2014).
[71] H. Yang, A. Zimmerman, A. Zenginoğlu, F. Zhang, E. Berti, and Y. Chen, Quasinormal modes of nearly extremal Kerr spacetimes: spectrum bifurcation and power-law ringdown, Phys. Rev. D **88**, 044047 (2013).
[72] A. Nagar, E. Harms, S. Bernuzzi, and A. Zenginoğlu, The antikick strikes back: recoil velocities for nearly-extremal binary black hole mergers in the test-mass limit, Phys. Rev. D **90**, 124086 (2014).
[73] S. A. Hughes, Evolution of circular, nonequatorial orbits of Kerr black holes due to gravitational wave emission. 2. Inspiral trajectories and gravitational wave forms, Phys. Rev. D **64**, 064004 (2001).
[74] T. Damour, B. R. Iyer, and A. Nagar, Improved resummation of post-Newtonian multipolar waveforms from circularized compact binaries, Phys. Rev. D **79**, 064004 (2009).
[75] A. Taracchini, A. Buonanno, S. A. Hughes, and G. Khanna, Modeling the horizon-absorbed gravitational flux for equatorial-circular orbits in Kerr spacetime, Phys. Rev. D **88**, 044001 (2013).
[76] A. Nagar and A. G. Shah, iResum: A new paradigm for resumming gravitational wave amplitudes, arXiv:1606.00207.
[77] L. Blanchet, A. Buonanno, and G. Faye, Tail-induced spin-orbit effect in the gravitational radiation of compact binaries, Phys. Rev. D **84**, 064041 (2011).
[78] L. Blanchet, A. Buonanno, and G. Faye, Third post-Newtonian spin-orbit effect in the gravitational radiation flux of compact binaries, arXiv:1210.0764.
[79] S. Marsat, L. Blanchet, A. Bohe, and G. Faye, Gravitational waves from spinning compact object binaries: New post-Newtonian results, arXiv:1312.5375.

[80] A. Bohé, G. Faye, S. Marsat, and E. K. Porter, Quadratic-in-spin effects in the orbital dynamics and gravitational-wave energy flux of compact binaries at the 3PN order, Classical Quantum Gravity **32**, 195010 (2015).

[81] E. Harms, G. Lukes-Gerakopoulos, S. Bernuzzi, and A. Nagar, Spinning test-body orbiting around Schwarzschild black hole: Circular dynamics and gravitational-wave fluxes, doi:10.5281/zenodo.61308 (2016).